A vacuum double-crystal spectrometer for reference-free X-ray spectroscopy of highly charged ions

P. Amaro, C. I. Szabo, S. Schlesser, A. Gumberidze, E. G. Kessler, A. Henins, E. O. Le Bigot, Martino Trassinelli, J. M. Isac, P. Travers, et al.

▶ **To cite this version:**

P. Amaro, C. I. Szabo, S. Schlesser, A. Gumberidze, E. G. Kessler, et al.. A vacuum double-crystal spectrometer for reference-free X-ray spectroscopy of highly charged ions. Radiation Physics and Chemistry, 2014, 98, pp.132-149. 10.1016/j.radphyschem.2014.01.015 . hal-01245577

HAL Id: hal-01245577
https://hal.science/hal-01245577v1

Submitted on 31 Aug 2020

HAL is a multi-disciplinary open access archive for the deposit and dissemination of scientific research documents, whether they are published or not. The documents may come from teaching and research institutions in France or abroad, or from public or private research centers.

L'archive ouverte pluridisciplinaire **HAL**, est destinée au dépôt et à la diffusion de documents scientifiques de niveau recherche, publiés ou non, émanant des établissements d'enseignement et de recherche français ou étrangers, des laboratoires publics ou privés.

A vacuum double-crystal spectrometer for reference-free X-ray spectroscopy of highly charged ions

P. Amaro [a,b,c,d,1], C.I. Szabo [b,c,d], S. Schlesser [b,c,d,2], A. Gumberidze [b,c,d,e,f], E.G. Kessler Jr. [g], A. Henins [g], E.O. Le Bigot [b,c,d], M. Trassinelli [h], J.M. Isac [b,c,d], P. Travers [b,c,d], M. Guerra [a], J.P. Santos [a], P. Indelicato [b,c,d,*]

[a] Centro de Física Atómica, CFA, Departamento de Física, Faculdade de Ciências e Tecnologia, FCT, Universidade Nova de Lisboa, 2829-516 Caparica, Portugal
[b] Laboratoire Kastler Brossel, Sorbonne Universités, UPMC Univ. Paris 06, Case 74; 4, place Jussieu, 75005 Paris, France
[c] Laboratoire Kastler Brossel, CNRS, 75005 Paris, France
[d] Laboratoire Kastler Brossel, Département de Physique de l'École Normale Supérieure, 24 Rue Lhomond, 75005 Paris, France
[e] ExtreMe Matter Institute EMMI and Research Division, GSI Helmholtzzentrum für Schwerionenforschung, D-64291 Darmstadt, Germany
[f] FIAS Frankfurt Institute for Advanced Studies, D-60438 Frankfurt am Main, Germany
[g] National Institute of Standards and Technology NIST, 100 Bureau Drive, Gaithersburg, MD 20899, USA
[h] Sorbonne Universités, Institut des Nanosciences de Paris, CNRS, UPMC, Univ Paris 06, 4, place Jussieu, 75005 Paris, France

We have built a vacuum double crystal spectrometer, which coupled to an electron-cyclotron resonance ion source, allows absolute measurements of low-energy X-ray transitions in highly charged ions with accuracies of the order of a few parts per million. We describe in detail the instrument and its performance. Furthermore, we present a few spectra of $n=2\rightarrow n=1$ transitions in Ar^{14+}, Ar^{15+} and Ar^{16+}. We have developed an *ab initio* simulation code that allows us to obtain accurate line profiles. It can reproduce experimental spectra with unprecedented accuracy. The quality of the profiles allows the direct determination of line width.

1. Introduction

The measurement of X-ray transition energies of highly charged ions (HCIs) is one of the main methods to test bound-state quantum electrodynamics (BSQED) effects in strong fields. BSQED has been intensively tested experimentally, yet recent measurements of the proton size in muonic hydrogen, which disagree by 7σ from measurements in normal hydrogen (Antognini et al., 2013; Pohl et al., 2010), show that its short distance behavior may not be as well understood as was believed up to now. Highly charged ions can be a very good testing ground for improving our understanding of BSQED.

Highly charged ions can be created, e.g., using high-energy accelerators, Electron Beam Ion Traps (EBIT), or Electron-Cyclotron Resonance Ion sources (ECRIS). Transitions between excited states and the $n=1$ ground state in few-electron atoms or ions have been measured in a number of elements ranging from hydrogen to uranium. For medium atomic number elements, relevant to X-ray reflection Bragg spectrometry (transition energies in the 2–15 keV range), accuracies in the few tens of parts per million range have been obtained. Beam-foil spectroscopy has been employed to provide measurements in hydrogenlike and heliumlike ions like phosphorus, sulfur, argon (Briand et al., 1983a) (80 ppm), iron

* Corresponding author at: Laboratoire Kastler Brossel, Sorbonne Universités, UPMC Univ. Paris 06, Case 74; 4, place Jussieu, 75005 Paris, France.
E-mail address: paul.indelicato@lkb.upmc.fr (P. Indelicato).
[1] Present address: Physikalisches Institut, Heidelberg University, D-69120 Heidelberg, Germany.
[2] Present address: KVI, Theory Group, University of Groningen, 9747 AA Groningen, The Netherlands.

(Briand et al., 1983b, 1984) (90 ppm) (Indelicato et al., 1986a) (25 ppm), germanium (Chantler et al., 2009) (14 ppm) and krypton (Indelicato et al., 1986b; Tavernier et al., 1985) (20 ppm). The main limitation to obtain high accuracy in Beam-foil spectrometry is due to the Doppler effect. Correction for the Doppler shift requires precise determination of the ions speed and angle of observation of the X rays emitted in flight. To get rid of this uncertainty, argon was also studied by X-ray spectrometry of recoil ions with an accuracy of 5 ppm (Beyer et al., 1985; Deslattes et al., 1984) relative to an X-ray standard. The uncertainty then was due to the presence of satellite lines associated with electron capture in the target gas. Another method to reduce the Doppler effect was to decelerate the beam after stripping it at high energy by capturing electrons from a gas cell, in the so-called "accel–decel" method. Hydrogenlike nickel was studied by this method (Beyer et al., 1991) with an accuracy of 13 ppm.

Devices like EBITs have been used to measure X-ray transitions in HCIs. Because the ions in EBITs have only thermal motion, no correction for Doppler shifts is required. Transition energies have been measured in hydrogenlike magnesium (Hölzer et al., 1998), hydrogenlike chlorine, hydrogenlike and heliumlike argon (Bruhns et al., 2007) and vanadium (Chantler et al., 2000). In Hölzer et al. (1998) and Bruhns et al. (2007), the hydrogenlike magnesium and chlorine Lyman α lines are measured without the use of X-ray reference lines, with an accuracy of 24 ppm and 10 ppm, respectively. The accuracy of the w line in He-like given to 2 ppm relative to the Lyman α was later improved to 1.5 ppm without the use of a reference line (Kubiček et al., 2012). In this work, the spectrometer used is made of a single Bragg crystal coupled to a CCD camera, which can be positioned very accurately with a laser beam reflected by the same crystal as the X-rays. More recently, a measurement of X-ray transition energies in heliumlike titanium was performed at an EBIT using a calibration based on neutral X-ray lines emitted from an electron fluorescence X-ray source. The value of the Lyman α was acquired with an accuracy of 15 ppm (Chantler et al., 2012).

Present day X-ray standards, as can be found in Deslattes et al. (2003), even though they are known with accuracies in the ppm range, are based on neutral elements with a K vacancy created by electron bombardment or photoionization. The shape and peak position of those lines depend on many factors like the excitation energy (see., e.g., Deslattes et al., 1982, 1983; Deutsch et al., 1996), the chemical composition and the surface contamination of the sample. Physical effects like shake-off, Auger and Coster–Kronig effects lead to multivacancies, which distort and broaden the line shape. Examples of the complex structure of Kα lines in transition elements can be found, e.g., in Deutsch et al. (2004, 1995) and Hölzer et al. (1997). It is thus very difficult to use these standard lines with their quoted accuracy. Therefore, it was recently proposed to use either exotic atoms (Anagnostopoulos et al., 2003b) or combination of exotic atoms and relatively cold, highly charged ions, produced in an ECRIS (Anagnostopoulos et al., 2003a) to provide reliable, reproducible, narrow, X-ray standard lines.

The first observation of strong X-ray lines of highly charged argon ions (up to He-like) in an ECRIS was made in 2000 (Douysset et al., 2000). This experiment led to the description of the mechanisms for the production of the different lines in the plasma (Costa et al., 2001; Martins et al., 2001). Since then, several experiments have been performed at the Paul Scherrer Institute (PSI), using a spherically curved crystal spectrometer and an ECRIS, (Anagnostopoulos et al., 2005; Indelicato et al., 2007, 2006; Le Bigot et al., 2009; Trassinelli et al., 2007) leading to improved understanding of the ECRIS plasmas for sulfur, chlorine and argon (Martins et al., 2009; Santos et al., 2010, 2008, 2011). Such lines can be used, e.g., to characterize X-ray spectrometers response functions (Anagnostopoulos et al., 2005). Yet specific techniques are required to measure their energy without the need for reference lines. The technique of Bruhns et al. (2007) and Kubiček et al. (2012), using a single flat crystal, is well adapted to the EBIT, which provides a very narrow (≈ 100 µm), but rather weak X-ray source. The ECRIS plasmas have been shown to be very intense sources of X-rays, but have diameters of a few cm. They are thus better adapted to spectrometers that can use an extended source. At low energies, cylindrically or spherically bent crystal spectrometers and double-crystal spectrometers (DCSs) can be used, but only the latter can provide high-accuracy, reference-free measurements.

Precision spectroscopy with double-crystal X-ray spectrometers has a long history. The first DCS was conceived and employed independently by Compton (1917), Bragg et al. (1921) and Wagner and Kulenkampff (1922) to measure absolute integrated reflections of crystals. Davis and Stempel (1921) used the DCS to study the width of the reflection curve. These experiments showed that the DCS was an instrument of high precision and high resolving power. They were followed by several others (see, e.g., Refs. Allison, 1932; Allison and Williams, 1930), and were instrumental in establishing the dynamical diffraction theory of Darwin (1914a,b) and Prins (1930). The capability of the dispersive mode to reach high-resolution was found by Davis and Purks (1927, 1928). The DCS was then used to obtain the K-line widths of some elements (Allison, 1933; Allison and Williams, 1930). A theoretical description of the instrument was provided by Schwarzschild (1928). A detailed technical description was given by Compton (1931) and Williams and Allison (1929). Williams (1932) introduced the vertical divergence correction in 1932, allowing for an improved accuracy for energy measurements. Bearden (1931a) provided an absolute measurement of copper and chromium K lines with the use of ruled gratings and calcite crystals in a DCS and deduced a value for the calcite lattice spacing, (Bearden, 1931b) leading the way to absolute X-ray wavelength measurements (Bearden, 1932). Detailed description of the instrument can be found in classic textbooks (Compton and Allison, 1935; James, 1948).

In a DCS, the first crystal, which is kept at a fixed angle, acts as a collimator, defining the direction and the energy of the incoming X-ray beam, which is analyzed by the second crystal. The first peak is obtained by scanning the second crystal angle when the two crystals are parallel (non-dispersive mode). Wagner and Kulenkampff (1922) were the first to show the absence of dispersion in the parallel mode. The peak shape depends only on the reflection profile of the crystals and provides the response function of the instrument. The second peak is obtained when both crystals deflect the beam in the same direction (dispersive mode). The peak shape is then a convolution of the line shape and of the instrument response function. The position of the first crystal is the same in both modes. The difference in angle settings of the second crystal between the non-dispersive and the dispersive modes is directly connected to the Bragg angle.

The DCS can be used in reflection (low-energy X-rays) in which case the energy that is being measured depends only on the Bragg angle, on the crystals lattice spacing d, on the crystal index of refraction and on the geometry (distance between the entrance and exit slits and height and width of the slits) of the instrument. In this case the reflecting planes are parallel to the surface of the crystal. In transmission (high-energy), there is no index of refraction correction, and the reflecting planes are perpendicular to the surface.

The DCS in both modes was used for many years to measure X-ray energies relative to standard lines, as the crystal lattice spacing was not known. This changed dramatically when high-quality Si and Ge high-purity single crystals became available, as they were needed for the fabrication of transistors. Interferometric

methods were then elaborated for direct measurement of the lattice spacing in terms of laser wavelength, (Becker et al., 1981; Bonse and Hart, 1965; Deslattes and Henins, 1973; Ferroglio et al., 2008; Hart, 1968; Massa et al., 2009a, 2009b; Okada and Tokumaru, 1984) with accuracies below 10^{-8}. The DCS became then a way to do reference-free measurements of X-ray wavelengths, using well-measured and characterized crystals as transfer standards. Deslattes (1967) designed a vacuum DCS intended for low-energy X-ray measurements, with high-precision angular encoders and rotating tables. A high-precision transmission instrument was constructed for high-energy X- and γ-ray, with angular interferometers able to measure angles to a fraction of milliarcseconds. This instrument is able to resolve inconsistencies between different determination of X- and γ-ray wavelengths (Deslattes et al., 1980; Kessler et al., 1979). DCSs have also been used to measure K lines of light elements like magnesium (Schweppe et al., 1994), copper (Deutsch et al., 1995), and of heavy elements like tungsten (Kessler et al., 1979) and from silver to uranium (Kessler et al., 1982). A complete tabulation of all available X-ray standards can be found in Deslattes et al. (2003).

The aim of the present paper is threefold. Firstly we describe a vacuum DCS for measuring low-energy X-rays, adapted to the use of an ECRIS plasma as an X-ray source, which provides specific constraints as the ECRIS cannot be moved, contrary to an X-ray tube, to be set to the correct position for a given Bragg angle. Secondly we discuss the performance and properties of a system composed of a DCS coupled to an ECRIS, and describe the *ab initio* simulation code that we have developed to reproduce and analyze experimental spectra. Finally, we describe a method, using the setup described above, to provide *absolute* measurements (i.e., without external theoretical or experimental reference) of line energies of inner-shell transitions in highly charged ions with an exceptional *accuracy*. These reference-free measurements use the known lattice spacing of a Si crystal as a transfer standard to tie X-ray wavelength to the definition of the meter, through the well-known realization using He–Ne lasers.

Reaching an accuracy of a few parts per million (ppm) in this context, this method can be used to probe and test QED (quantum electrodynamic) effects such as two-loop self energy corrections and provide new, more reliable X-ray standards in the few keV energy region (Anagnostopoulos et al., 2005, 2003b).

This paper is organized as follows: in Section 2 we describe the technical features of the ECRIS and the DCS and their alignment. We also describe the measurement of the lattice spacing of the crystals that are used by the DCS. In Section 3 we give a brief review of the Monte-Carlo simulation used in this work. We discuss the experimental procedure in Section 4 and how one can assess the accuracy of measurements performed with a DCS in Section 5. In Section 6 we present an example of measurements and experimental tests performed with this experimental setup. The conclusions are presented in Section 7.

2. Experimental setup

2.1. ECRIS

An electron-cyclotron resonance ion source is a device built around a minimum-B structure, designed to trap hot electrons. This structure is composed of a magnetic bottle for longitudinal trapping that can be made of coils or permanent magnets. The transverse trapping required in such a structure is performed with a multipole magnet, e.g., in our case a permanent magnet hexapole. Microwaves are injected in a plasma chamber inside this structure, at a frequency resonant with the electrons cyclotron frequency on a constant $|\boldsymbol{B}|$ surface, which resembles an ellipsoid. The electric field of the microwaves can then accelerate electrons to very high energies. A gas or vapor is injected inside the plasma chamber and the atoms are then ionized and trapped in the space charge of the electrons, which have a density in the order of 10^{11} cm^{-3}. The plasma is subject to an electric field through a *polarization electrode*, which helps to optimize ion production. Ion beams can be extracted along the symmetry axis of the magnetic bottle by applying a high voltage on an extraction electrode. A general description of an ECRIS can be found in, e.g., Geller (1996).

The Source d'Ions Multichargés de Paris (SIMPA) is a "supernanogan" ECRIS constructed by the Pantechnik Company (Bieth et al., 2000). The magnetic structure is made of permanent magnets, with field strength up to 1.3 T on the surface of the magnet. The microwave frequency is 14.5 GHz, produced by a 2 kW klystron. This source has been jointly operated by the Laboratoire Kastler Brossel (LKB) and the Institut des NanoSciences de Paris (INSP) since 2004. Numerous projects that use the extracted beam and the X-ray radiation of the ECRIS plasma have been started in atomic, plasma and surface physics (Gumberidze et al., 2009, 2010). SIMPA has been modified to allow for observation of the plasma through the polarization electrode. A sketch of the SIMPA ECRIS is presented in Fig. 1.

The source has been fully characterized (electronic and ionic densities, electronic temperature, X-ray production) using X-rays and extracted ion beams (Gumberidze et al., 2010). One consequence of the ion creation and excited level population mechanisms described in Costa et al. (2001), Martins et al. (2001, 2009) and Santos et al. (2010, 2008, 2011) is that the $1s2s\,^3S_1$ level in He-like ions is strongly populated. It is created by inner-shell ionization of the Li-like ion ground state $1s^2 2s$. Other excited levels of He-like ions, populated by excitation of the $1s^2$ ground state or by ionization and excitation mechanisms, are much less populated. This leads to the observation of a very strong $1s2s\,^3S_1 \rightarrow 1s^2\,^1S_0$ M1 transition, which is very forbidden, having a radiative width of only 10^{-7} eV for argon. At the same time, the ions in the ECRIS are rather cold. They are trapped in the potential created by the space charge of the electrons. In SIMPA the plasma is close to a sphere of 3 cm in diameter. Assuming a uniform electron charge density of 10^{11} cm^{-3}, one easily gets a potential depth of 0.27 eV and a Doppler broadening of 95 meV. Conversely, the measured broadening of 80 meV for the M1 line of He-like argon (Amaro et al., 2012) corresponds to an electron density of 7.2×10^{10} cm^{-3} and to a potential depth of 0.195 V (see also Szabo et al., 2013, 2012).

In contrast, HCIs in an EBIT have higher temperatures due to a deeper trap. The ion temperature in an EBIT was measured recently in Heidelberg and was found to be 6.9 eV (Soria Orts et al., 2007) after evaporative cooling and for an electron beam current of 20 mA. This process further reduces the number of ions that can be used for spectroscopy. A detailed study of this cooling technique was recently performed in a laser spectroscopy experiment on

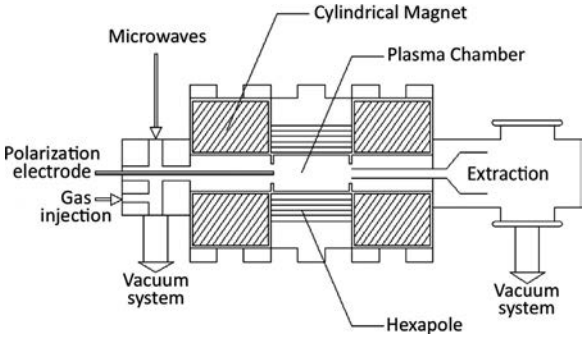

Fig. 1. Schematics of the SIMPA ECRIS.

Ar^{13+} (Mäckel et al., 2011) in which a final temperature of 28 eV after evaporative cooling was measured.

Observation and measurement of the $1s2s\,^3S_1 \rightarrow 1s^2\,^1S_0$ M1 transition offers a *unique* opportunity to fully characterize a spectrometer. For argon, for example, the Doppler-broadened M1 transition is ten times narrower than the width of the Kα transitions in core-excited argon (0.79 eV) (Campbell and Papp, 2001). In the case of the DCS, for which the response function can be calculated from first principles, we can thus compare quantitatively the experimental profile and the simulated one and check the quality of the crystals.

The geometry of the SIMPA ECRIS has some influence on the positioning of the spectrometer. Fig. 2 shows the distances between the plasma, the different parts and the first crystal. A picture of the installation from the source side is shown in Fig. 3. The installation of a collimator is needed to reduce the background, due, e.g., to X-rays that get to the crystal without passing inside the polarization electrode. Because of the collimator and polarization electrode, the X-ray beam that hits the first crystal has an angular aperture of $\pm$ 6°. The Be window which isolates the vacuum of the source from the primary vacuum in the spectrometer has a transmission varying from 61% at 3091 eV to 65% at 3135 eV, an energy range that corresponds to the observation of the $1s2s^22p\,^1P_1 \rightarrow 1s^22s^2\,^1S_0$ transition in Be-like argon to the $1s2p\,^1P_1 \rightarrow 1s^2\,^1S_0$ transition in He-like argon.

All the experiments to date with this setup were performed with few-electron argon ion X-rays. The microwave power injected in the source was between 250 W and 350 W. A support gas, oxygen, was injected simultaneously with argon to provide electrons. The pressure, measured at the injection side of the ECRIS (see Fig. 3) was between 3×10^{-5} mbars and 8×10^{-5} mbars. A quadrupole mass spectrometer, positioned on the extraction side of the ECRIS, provides information on the exact composition of the gas in the source, to improve the reproducibility of the ECRIS tuning.

2.2. Double crystal spectrometer

The most characteristic aspect of the DCS at SIMPA, compared to other double crystal instruments such as the one located at NIST (National Institute of Standard and Technology) (Deslattes, 1967), is that both crystal axes are mounted on a single support table that rotates around the first crystal axis (Fig. 4). In other DCSs, the crystals are fixed on a steady platform with the X-ray source having a rotation axis concentric with the first crystal axis (Deslattes, 1967). The X-ray source can then be rotated so that the X-rays impinging on the first crystal meet the Bragg condition and are refracted toward the second crystal.

In this experiment, the X-ray source is a massive, complicated device with several tons of fixed components (vacuum system, magnets, beam line), which makes its rotation impossible. In the design of our DCS, a heavy table supports both crystal axes, and can be rotated to adjust the instrument to an arbitrary energy range. Fig. 5 shows an overall view of the spectrometer with all the

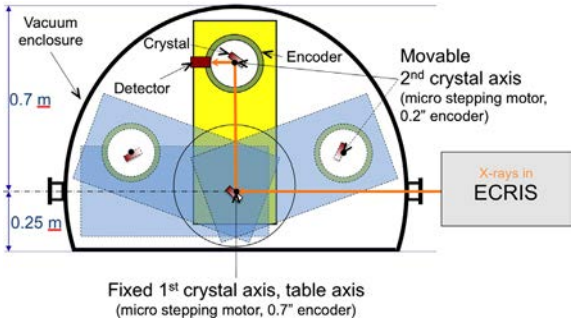

Fig. 4. Scheme of the DCS.

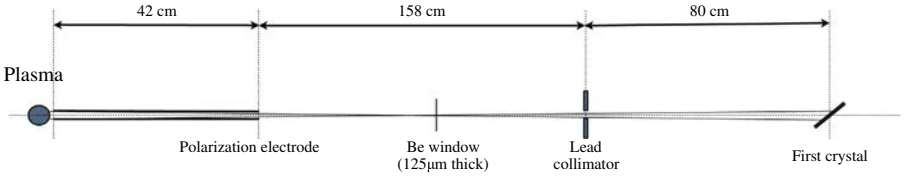

Fig. 2. Geometrical arrangement of the DCS, polarization electrode, lead collimator and of the SIMPA ECRIS plasma. The inner diameter of the polarization electrode is 12 mm.

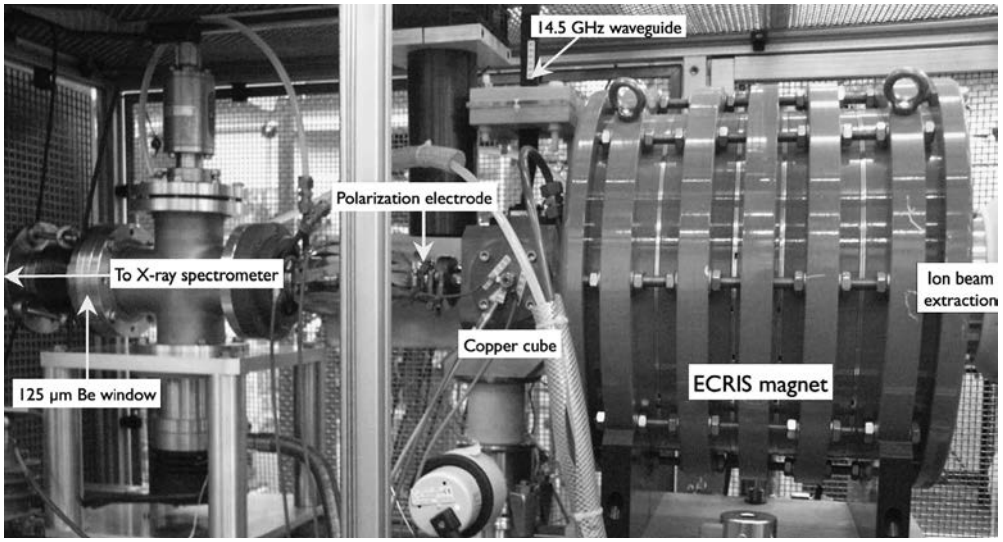

Fig. 3. The SIMPA ECRIS and its connection to the spectrometer.

major components and Fig. 6 shows a picture of the spectrometer components.

Both crystal supports are mounted on a single horizontal table (Fig. 5,8), 6 cm thick and weighing $\approx$200 kg. Both supports are built so that the crystals rotate around a vertical axis (Figs. 5, 2 and 3) passing through the center of the front surface of each crystal. The spectrometer table and the rotating table supports are made of a special alloy, LK3 (0.4% C, 1.8% Cr, 1% Al, 0.25% Mo), chosen for its long-term stability. We used material that was forged at a temperature of 1100 °C and a stabilized at 900 °C for 48 h. After machining, the different parts have been submitted to a stabilization annealing at 825 °C for 24 h to release strains in the material. The parts have then been finished by grinding the different surfaces to 2 μm accuracy to insure excellent parallelism of the two axes. The first crystal support weighs 63 kg and the second one 80 kg.

The spectrometer table is mounted on a heavy-duty indexing table (Figs. 5, 9), able to support the weight of the spectrometer assembly ($\approx$360 kg), and rotate it to an arbitrary angle. The assembly rotates around the same vertical axis as the first crystal axis. The indexing table is directly fixed to the lower flange of the vacuum chamber, on a surface that has been precisely machined. Because the spectrometer table is not centered on the indexing table, it is supported by a pair of conical wheels with precision ball bearings. The conical part of the wheels (Figs. 5, 10) has been ground to provide excellent contact. The conical wheels roll on a metallic track (Figs. 5, 11), resting on the lower vacuum chamber flange, with a system of adjustment screws. Both the track and the cone surfaces have been hardened. The wheel positions can be adjusted to compensate for the table weight. The vacuum chamber weighs more than 1000 kg. It is placed on a support table with adjustable anti-vibration feet. The whole chamber can be moved for alignment with translation stages (Figs. 5, 13) made of two flat greased metallic pieces. Four screws (Figs. 5, 16) allow for a precise positioning of the chamber during alignment. The support table itself (Figs. 5, 14) rests on the ground with adjustable anti-vibration feet. The chamber can be pumped down to a primary vacuum of 10^{-2} mbar that reduces the absorption of the low energy X-rays (around 3 keV), while being in a range of the Paschen curve for air where the detector high-voltage (2 kV) does not spark.

The rotation of the crystals is performed with precision stepping motors powered by a three-axis micro-stepping controller Newport ESP301-3G, able to perform rotations as small as 0.017 in. A Huber model 410 rotation stage is used for the first crystal, a Newport RV80PP for the second crystal and a Newport RV240PP for the detector. The angle of the first crystal is measured with a Heidenhain ROD800 encoder with a sensitivity of 0.01 in. Absolute angle is known with 0.5 in accuracy over a full turn. The electronic control system uses the digital signal provided by the encoder to maintain the position of the crystal to the set angle over long periods of time. When the angle drifts too far away from the set position, the system stops counting X-rays until the feedback control brings the angle back to the set position. For the data analysis, we use the average first crystal angle, and the standard deviation is used to define the uncertainty. The measured value for the first axis angle standard deviation ranges between 0.014 in and 0.065 in. These position fluctuations have a very small contribution to the total error budget. The second crystal angle is measured to a precision of 0.2 in with a Heindenhain RON905 encoder, using a Heidenhain AWE1024 controller for data processing. During data acquisition, the second crystal rotates continuously at a roughly constant speed. Fluctuations in the step size however, due to backlash in the gears and non-uniformity in the stepping motor magnetic field, lead to small variation of the time spent in each bin. The scanning range is divided into a number of bins of identical size (typically 100 bins of 5.7 in). The counts are stored

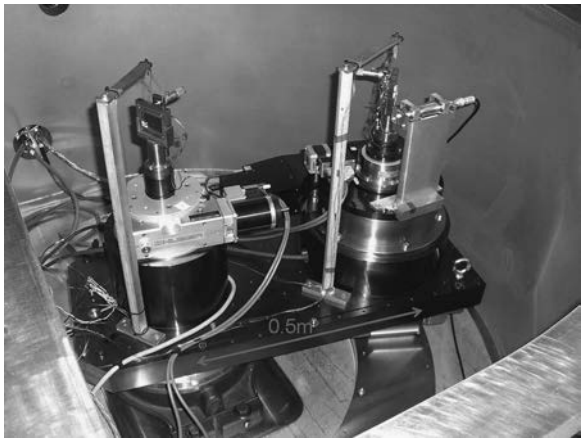

Fig. 6. General view of the spectrometer.

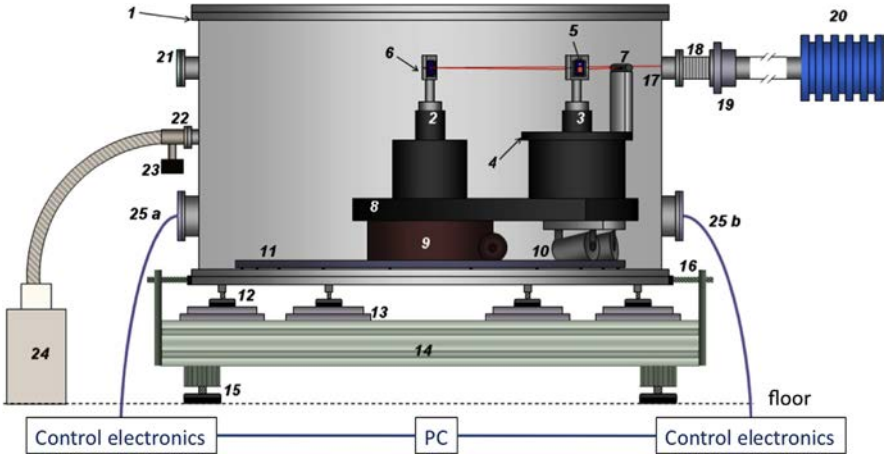

Fig. 5. Spectrometer setup: (1) vacuum chamber; (2) axis #1 (first crystal support with rotation stage and angular encoder); (3) axis #2 (second crystal support, rotation stage, encoder); (4) X-ray detector rotation stage ; (5) crystal on second axis; (6) first axis crystal holder; (7) X-ray detector; (8) spectrometer table; (9) spectrometer table rotation stage; (10) conic wheels; (11) tracks for wheels; (12) vacuum chamber anti-vibration feet with vertical positioning; 13) translation stages; (14) spectrometer support table; (15) anti-vibration feet with vertical positioning; (16) positioning screws; (17) X-ray entrance; (18) bellows; (19) Be window; (20) SIMPA ECRIS; (21) optical window; (22) bellows connection to vacuum pump; (23) pressure gauge and valve; (24) primary vacuum pump; (25) a and b flanges equipped with feedthroughs for cables and cooling water.

in a bin when the angle value measured by the encoder is contained between the minimum and the maximum angle defined for the bin. The content of each bin is divided by the time spent in the bin to insure proper normalization. The time during which the first axis wanders too far away from the set position, leading to a stop in X-ray collection, is measured and subtracted from the acquisition time for a given bin. In a typical spectrum, the time spent in a bin is around 13.5 s and can fluctuate between 10 s and 17 s. A typical spectrum is recorded in 10 min in the parallel mode and in 20 min in the dispersive mode.

A xenon (90%) and methane (10%) gas filled proportional counter detector is mounted on a Newport RV 240PP rotation stage with an axis of rotation concentric with the second crystal vertical axis. The detector has a 50 μm thick Be window and has an active area of about 12×25 mm^2. The detector is operated at a high voltage of about 2000 V with and external power supply. The detector signal is processed by an ORTEC 142PC low noise charge-sensitive preamplifier and an ORTEC 572 spectroscopy amplifier with a shaping time of 6 μs. An ORTEC window and scalar module is used to generate TTL pulses when the signal amplitude corresponds to the expected X-ray energy. These pulses are accumulated by a 6602 PC card from National Instruments. A Labview program pilots the microstepping motor control unit for both axes and detector rotation stages. The same program reads the AWE 1024 controller through a GPIB bus and the first crystal encoder with an Heidenhain IK 220 PC card. The program uses the reading from the first axis encoder to maintain the angle, while scanning the second axis angle and acquiring the counts from the 6602 card. The program displays and updates a plot of the crystals angular positions and of the spectrum recorded during a complete measurement cycle.

The temperature of the crystals is measured to 0.1 °C accuracy using a calibrated Pt100 thermistor. This thermistor is also used to regulate the temperature of the crystal. A heating element is pressed between two thin copper plates, which are applied to the back of the crystal (Fig. 8). A 100 μm thick soft graphite foil assures a good thermal contact between the crystal and the Cu plate in vacuum. Water-cooling is applied to the rotary stages stepping motors, in order to provide sufficient heat loss when the spectrometer is under vacuum. A feedback loop controls the power in the heating element using a proportional-integral-derivative (PID) controller. The maximum allowed fluctuation in the course of one measurement is 0.2 °C. The temperature of both crystals is also recorded during the scans with each data point registered in the data files.

2.3. Alignment procedure

The DCS must be carefully aligned with respect to the SIMPA axis to optimize the spectrometer throughput and to allow finding easily the lines that are to be measured. The quality of the vertical alignment is very important for reducing systematic errors. The procedure is the following. First, two carefully machined cylindrical pieces with crosshairs are placed on the flanges at the exit of the source in place of the Be window (see Fig. 3) and at the end of the beam line on the other side of the source (on the alignment port of the 1.5 tons dipole magnet Fig. 7a). Both ports have been aligned with the source before. A theodolite equipped with angular encoders of arcsecond accuracy and with an electronic tilt-meter is then positioned so that it is on a straight line with respect to the crosshairs. The horizontality of the axis can be verified to a few seconds of arc using the tiltmeter. The spectrometer chamber is then equipped with crosshairs on the entrance and exit flange. The theodolite is then used to align horizontally and vertically the chamber. A lead diaphragm, slightly smaller than the detector entrance window, is installed on the entrance port of the spectrometer chamber, and its alignment is checked. The spectrometer table is then rotated so that both crystal supports are aligned with the source axis. An alignment laser is then set to go through the crosshairs (see Fig. 7a–d). A high-quality mirror is installed in place of the second crystal. The axis is then rotated until the laser is reflected back onto itself. The verticality of the mirror is adjustable (Fig. 8). The crystal support rotates on an axis going through the front surface of the mirror, using a system of flexure hinges (Paros and Weisbord, 1965) and a micrometric screw. The support surface is ground to 2 μm accuracy. This enables the substitution of the mirror by a crystal without losing the vertical alignment. The accuracy of this alignment is defined

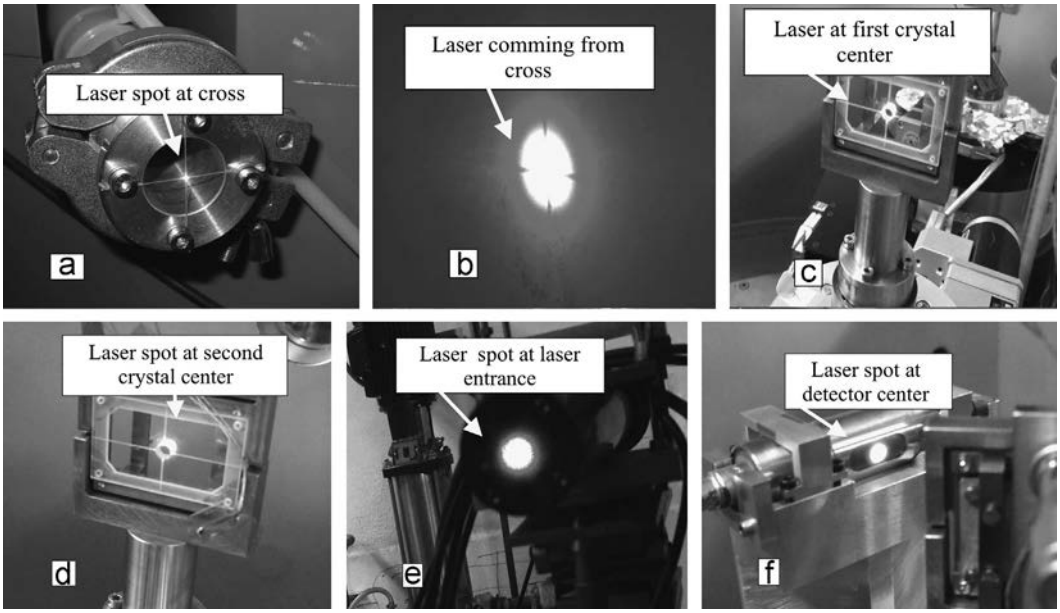

Fig. 7. The laser beam is aligned with (a) cross located at the backside of the ECRIS source; (b) the cross located at front side of the ECRIS source (b is a picture of the outgoing laser on a screen); (c) the center of the first crystal; and (d) the center of the second crystal. Then, a high-quality mirror is inserted in place of the second crystal. The encoder offset is set by making the laser beam go back to the starting point (e). After moving the table, the second crystal is set in the measurement position and the detector is aligned with the laser (f).

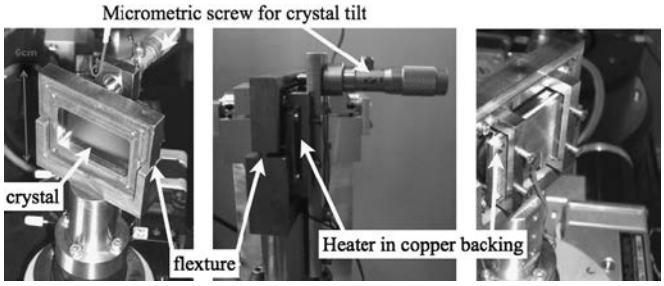

Fig. 8. Details of the crystal support, with the vertical tilting system (composed of a flexure and a micrometric screw) and the heater plate for temperature control. The copper plate ensures uniform repartition of heat on the back of the crystal. A graphite foil is positioned between the crystal and the copper plates to improve thermal contact under vacuum.

by the precision with which the laser beam can be centered when reflected back onto itself (see Fig. 7e). This is around 2 mm over a distance of 16 m, i.e., 13 s of arc. The angle on the encoder of the second crystal axis is then set to 90° to provide an logical reference angle for the measurements.

Once the second crystal support is aligned, the same procedure is repeated on the first crystal support. At this point, both mirrors are parallel to each other and perpendicular to the source axis. This is called the nominal alignment position. The first crystal is then rotated to the Bragg angle value corresponding to the transition to be measured, and the spectrometer table is rotated until the laser beam hits the center of the second mirror and is reflected back onto itself. The second crystal is then rotated to the Bragg angle so that both mirrors are parallel. The X-ray detector is then positioned on the laser beam to mark the detector position for the parallel or non-dispersive mode (see Fig. 7f). Finally the second crystal is rotated so that it is at the correct Bragg angle for the dispersive mode and the detector is moved to the correct position to check if it is correctly centered on the laser beam and to mark its position in the non-dispersive mode.

The horizontality of the various components was checked with a Wyler Clino 2000 tiltmeter to a precision of a few seconds of arc, and the verticality of the crystals with a Wyler Zerotronic sensor to the same accuracy. The mirrors are then replaced by the crystals. The crystals are brought into contact with the reference surface of the support, which is the same surface against which the mirrors were set. Four nylon screws are used to gently push the crystals against this surface and maintain them without strains (Fig. 8). By comparing simulations with experimental data (cf. Sections 5 and 6) we estimate the bending of the crystals due to this method of support to be negligible. Once this procedure is completed, the spectrometer is ready for actual measurements. The ECRIS is started, and an X-ray picture is taken in front of the first crystal to check that it is uniformly illuminated. The total uncertainty associated with the alignment procedure is 0.01°. The procedures used to check this alignment are presented in Sections 5 and 6.

2.4. Crystals preparation and measurement

In order to obtain an absolute energy measurement with the DCS, it is necessary to know the crystal lattice spacing with high accuracy. Four silicon crystals have been manufactured at NIST for the Paris DCS, two with Miller indices (111) and two with (220). Polishing procedures that lead to optical-quality surfaces (e.g., diamond powder polishing) damage the crystal surface and are not satisfactory for obtaining high-quality crystals for X-ray spectroscopy. Chemo-mechanical polishing (CMP) has been shown to lead to a somewhat broader distribution of lattice spacing values (Deslattes et al., 1999). The crystals were attached to a support with wax, oriented using a crystal X-ray spectrometer and lapped, using SYTON, a colloidal silica slurry. The lapping was performed so that the cut angle (angle between crystal planes and crystal surface) is smaller than 10 arc s to reduce asymmetric cut corrections to a negligible value (James, 1948). The crystals were then etched to remove strains and surface damages and minimize lattice spacing dispersion. The crystals have thus a slightly frosted aspect, making the surface rather diffusive for laser light.

2.4.1. Description of the measurement

All four crystals were cut from a boule obtained from Wacker–Siltronic. A small test crystal was prepared from the same boule for measurement of the lattice spacing, using the so-called "delta-*d*" spectrometer from NIST (Kessler et al., 1994). The physical separation between the "delta-*d*" diffraction crystal and the DCS diffraction crystals was kept as small as possible so that any variation in lattice spacing along the boule will have negligible influence on the determination of the lattice spacing of the DCS diffraction crystals. Although it is expected that the lattice spacings of the two samples are identical, a relative uncertainty component of 10^{-8} is included in the lattice spacing uncertainty to account for possible sample-to-sample variations (Kessler et al., 1999). The "delta-*d*" crystal was cut from a 18 mm × 12 mm × 6 mm sample with a thin lamella for diffraction as the top half and a base for mounting as the bottom half. The "delta-*d*" crystal was etched to a lamella thickness near 0.450 mm, which was determined by fitting the "delta-*d*" machine spectra with theoretical diffraction profiles.

The test crystal was attached to a PZT tipper using soft wax and the crystal/PZT tipper assembly was mounted on the "delta-*d*" translation sled. Another sample crystal, the reference crystal, cut from the WASO04 silicon boule, was also mounted on the translation sled. The WASO04 boule, also grown by Wacker–Siltronic, is a nearly perfect single crystal natural silicon material that was specifically grown for the International Avogadro Project (Andreas et al., 2011; Fujii et al., 2005; Kessler et al., 1994, 1999; Massa et al., 2011; Mohr et al., 2008). The lattice spacing of the WASO04/NIST reference crystal was determined as part of the International Avogadro Project (Massa et al., 2011).

The comparison measurements were recorded in the period from January 9 to 23, 2006. The relative difference in lattice spacing between the DCS test crystal and the WASO04/NIST reference crystal was measured as well as the variation in lattice spacing over the central 6 mm wide area of the DCS crystal.

2.4.2. Result of lattice comparison measurement

The "delta-*d*" spectrometer measures the small differences in Bragg angle between two crystals, from which the lattice spacing difference of the two crystals is inferred. Silver Kα radiation is diffracted in a two-crystal transmission non-dispersive geometry and the recorded profiles are fit with theoretical dynamical diffraction profiles. A complete description of the spectrometer and the measurement procedures is available in Kessler et al. (1994).

Profiles were recorded with the second crystal position alternately being occupied by the test and the reference crystal. The first crystal was rotated both clockwise and counterclockwise. Temperatures of the first crystal and of the test and reference crystals were measured at each data point and small corrections for temperature are made to the raw data before fitting. Over a 24 h period, typical temperature changes of about 0.010 °C were noted.

The data used to obtain the lattice spacing difference between the two crystals included 150 data scans recorded over 10 days. The measured lattice spacing difference is $(d_{\text{test}} - d_{\text{Ref.}})/d_{\text{Ref.}} = (-2.3 \pm 0.5) \times 10^{-8}$ where the uncertainty includes a statistical component (2×10^{-9}) and systematic

components associated with crystal temperature measurements (3×10^{-9}), crystal alignment (10^{-9}), and location of X-ray paths and crystals (3×10^{-9}).

In order to take into account variations along the Wacker–Siltronic boule, we include a relative uncertainty component of 10^{-8} and convert the measurement reported in the previous paragraph to the final result for the DCS spectrometer crystals $(d-d_{\mathrm{WASO04/NIST}})/d_{\mathrm{WASO04/NIST}}=(-2.3\pm1.1)\times10^{-8}$.

The variation of the lattice spacing along the surface of the DCS test crystal was measured by comparing the central region with the ±3 mm regions surrounding it. The relative change in lattice spacing along this 6 mm region was measured to be 8.6×10^{-9}. This variation is consistent with the 10^{-8} relative uncertainty component that has been attributed to the lattice parameter variation along the Wacker–Siltronic boule.

2.4.3. Absolute lattice parameter value

There have been several new measurements of the d_{220} lattice spacing of natural silicon in the past 5 years (Massa et al., 2009a,b). In addition, the lattice parameter of an ideal single crystal of naturally occurring Si, free of impurities and imperfections is one of the quantities that is determined in the CODATA recommended values of the fundamental physical constants. The variation of the d_{220} value between the 2006 (Mohr et al., 2008) and 2010 (CODATA, 2011) CODATA recommended values is more than 3 times the stated uncertainty. In order to compare lattice parameter values of different crystals, corrections for measured C, O, and N impurity concentrations are taken into account. From this collection of lattice parameter values, a straightforward approach to an absolute lattice spacing value for the WASO04/NIST reference crystal is not obvious.

Fortunately, in a 2011 publication a d_{220} value for the specific WASO04/NIST reference crystal was determined (Massa et al., 2011). The lattice parameter of a sample taken from a specific location (87 cm from crystal seed) in the WASO04 boule was carefully measured. Then corrections were made for the variation in the C, O, and N impurity concentrations along the WASO04 boule to determine the lattice spacing of the WASO04/NIST reference crystal (143 cm from the crystal seed). The value of the lattice spacing of the WASO04/NIST reference crystal is $d_{220}=192.0143374(10)\times10^{-12}$ m in vacuum at 20 °C. The relative uncertainty of this value is 0.5×10^{-8}. This value can be adjusted to the laboratory temperature by using the expansion expression for natural silicon

$$\frac{\Delta d}{d}=\eta_0(T-20)+\eta_1(T-20)^2, \tag{1}$$

where T is the laboratory temperature in °C, $\eta_0=2.5554\times10^{-6}\,^{\circ}\mathrm{C}^{-1}$, and $\eta_1=4.58\times10^{-9}\,^{\circ}\mathrm{C}^{-2}$ (Schödel and Bönsch, 2001). At 22.5 °C in vacuum, the WASO04/NIST reference crystal lattice spacing is $d_{220}=192.0155696(10)\times10^{-12}$ m.

Finally, the measured lattice spacing difference between the WASO04/NIST reference crystal and the DCS crystal material is used to calculate the absolute lattice spacing of the DCS crystals $d_{220}=192.0155651(23)\times10^{-12}$ m and $d_{111}=313.5601048(38)\times10^{-12}$ m in vacuum at 22.5 °C. The results and uncertainties for the Si (220) crystals are summarized in Table 1. When these crystals are used in a laboratory environment for diffraction measurements, the above lattice parameter values should be adjusted for the temperature of the crystals and the laboratory air pressure. The expansion correction is given in Eq. (1) and the compressibility correction is

$$\frac{\delta d}{d}=-\varepsilon p, \tag{2}$$

Table 1
Lattice spacing value for the Si (220) crystals of the spectrometer at 22.5 °C in vacuum. The Si (111) values can be deduced by multiplying with the factor $\sqrt{8/3}$. Numbers in parenthesis are uncertainties.

Crystal/Measurement	Value (Å)	Relative accuracy (ppm)
WASO04/NIST reference crystal (22.5 °C, vacuum)	1.920155696(10)	0.005
"delta-*d*" measurement	−0.000000045(21)	0.011
DCS Si (220) crystals (22.5 °C, vacuum)	1.920155651(23)	0.012

where p is the laboratory pressure in atm, $\varepsilon=3.452\times10^{-7}$ atm^{-1} (McSkimin, 1953; Nye, 1957). For a pressure of 1 atm, the relative correction is approximately -3.4×10^{-7}.

3. Simulation of the DCS

We have developed a ray-tracing program to obtain theoretical line profiles for the DCS, in the dispersive and non-dispersive modes. The results of this simulation program are used to analyze the experimental data. The program is based on the Monte-Carlo method and includes all relevant geometrical components of the experiment, as shown in Fig. 2, along with the crystal reflectivity curve calculated by dynamical diffraction theory (see, e.g., Zachariasen, 1967) using XOP (Sanchez del Rio and Dejus, 2004a, b, 1998) and checked with X0h (Lugovskaya and Stepanov, 1991, Stepanov). This makes the simulation code capable of taking into account multiple reflections in the crystal and corrections to the Bragg law, such as the index of refraction corrections and energy-dependent absorption. The simulation can be run with specific distribution functions around a given X-ray energy, to take into account the natural width (Lorentzian profile) or Doppler broadening (Gaussian profile) or both (Voigt profile). The simulation is thus also capable of providing a line-width analysis for our experimental spectra. A line profile is represented by the number of rays hitting the detector as a function of the second crystal angle. This line profile is sometimes called the rocking curve (Allison, 1932).

The non-dispersive profile, represented by $(n_1, -n_2)$ in Allison's notation (Allison and Williams, 1930), where n_i is the order of diffraction on the ith crystal, is obtained by scanning the second crystal in the case in which both crystals are parallel, as shown in Fig. 9(a). This profile is called non-dispersive since each bin in the rocking curve has contributions from all wavelengths accepted by the first crystal and reaching the second crystal. The peak in this profile indicates that the crystallographic planes of both crystals are parallel.

The dispersive profile noted as $(n_1, +n_2)$ which corresponds to the geometry represented in Fig. 9(b) provides a peak for the case of a (quasi)monochromatic incoming X-ray line. The peak profile in this case is a convolution product of the instrument response function and the natural line shape. The observed intensity in this configuration is much lower than in the $(n_1, -n_2)$ configuration, as each angle corresponds to only one wavelength, within the width of the crystals' reflectivity curve. Up to now we have only performed measurements in the first order, so we will restrict our analysis to the $(1, -1)$ and $(1, +1)$ cases.

The vertical geometry of the DCS in the nominal alignment position is shown in Fig. 10 to demonstrate the vertical divergence angle ϕ and the crystal tilt angles δ_1 and δ_2 used in the simulation. A succession of three *xyz* (orthogonal) coordinate systems is defined that follows the central line in the simulation (see Fig. 11). Each randomly generated ray will be represented in these coordinate systems within the three different parts of the

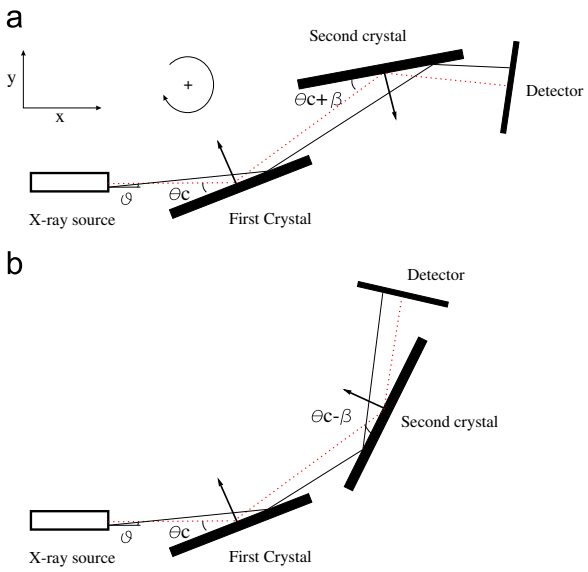

Fig. 9. Geometry of the DCS in the horizontal plane. (a) and (b) refer to the non-dispersive and the dispersive position respectively. The dotted line defines the central beam named "central line" in the simulation model. θ is the horizontal deviation of the X-rays compared to the central line, θ_C is the central line's angle with respect to the first crystal and $\theta_C \pm \beta$ is the central line's angle with respect to the second crystal in the non-dispersive and dispersive modes respectively. The crystallographic planes of the crystals are defined by their normal vectors.

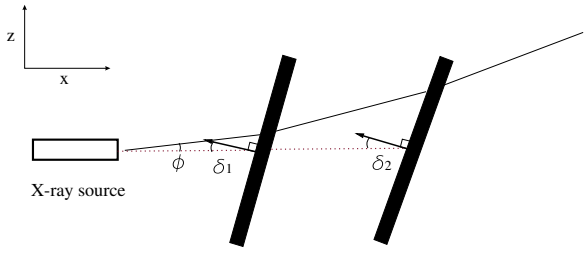

Fig. 10. Geometry of the DCS in the vertical plane in the nominal alignment position (see Section 2.3) when the spectrometer table is placed to be parallel to the axis of the source and the crystals are rotated to be perpendicular to this same axis. This is not an actual measurement position, but serves as an example for the crystal tilts and the beam. The dotted line defines the central beam (or central line) used in the simulation model. ϕ is the vertical divergence angle of the X-ray beam at the source, δ_1 and δ_2 are the vertical tilt angles of both crystals. (The tilts and vertical divergence angles are exaggerated on this figure.).

experiment. The three coordinate systems are shown for the non-dispersive case in Fig. 11. The central line that is the line connecting the geometrical centers of the different components of an ideally aligned spectrometer defines the x, x_a, x_b axes of the three successive coordinate systems.

Misalignments of successive components of the experiment defined in Figs. 9 and 10 are taken into account in the simulation with respect to these three ideal *xyz* coordinate systems shown in Fig. 11. We define the angle θ_T as the horizontal angle between the ion source axis and the plane defined by the two crystal axes. When the experiment is properly set, we should have $\theta_T \approx 2\theta_C$ and $\theta_C \approx \theta_B$, the Bragg angle (see Fig. 9 for the other definitions).

A simulated rocking curve is calculated using $\approx 10^6$ rays, each defined by generating a set of three *xyz* coordinates and two angles ϕ and θ with a uniform random generator, for successive values of the scanning angles β. A simulated spectrum is created by counting the number of X-rays reaching the detector for a given value of β. In order to save computer time the values of ϕ and θ are constrained in the range $(U[\theta_{min}, \theta_{max}], U[\phi_{min}, \phi_{max}])$, where the angles θ_{min}, θ_{max}, ϕ_{min} and ϕ_{max} are given by the successive collimators between the source and the first crystal (see Fig. 2).

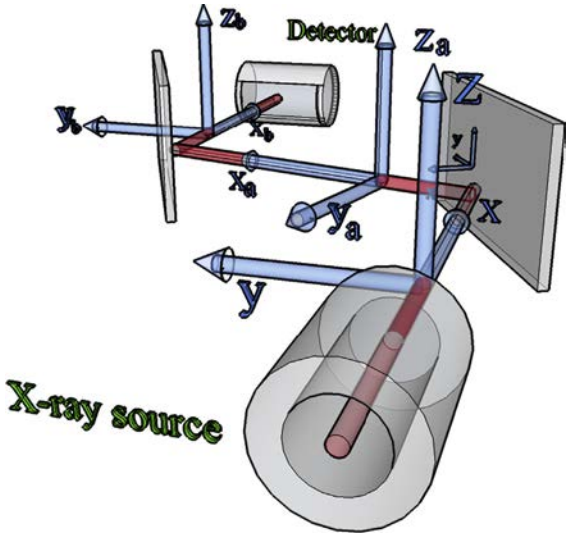

Fig. 11. Geometry of the DCS in the non-dispersive setup with the tri-orthogonal *xyz* axis along the central line.

The ray direction is expressed by the Cartesian components of the unitary vector $\hat{\boldsymbol{e}}$:

$$\begin{aligned} \hat{e}_x &= \cos(\phi)\cos(\theta), \\ \hat{e}_y &= \cos(\phi)\sin(\theta), \\ \hat{e}_z &= \sin(\phi). \end{aligned} \tag{3}$$

Furthermore, the initial position yz at the source exit is defined by a fixed uniform random distribution $(U[-R_c, R_c], U[-R_c, R_c])$, where R_c is the source tube radius. If a position is generated outside the region $y^2+z^2 < R_c^2$, it is discarded and another point is generated. This procedure was used for saving computer time since evaluation of trigonometric functions is minimized.

The position of the ray at the crystal in the plane $y'z'$, perpendicular to the source axis, which includes also the first crystal axis of rotation, is given by

$$\begin{aligned} y' &= y + L\tan(\theta), \\ z' &= z + L\tan(\phi), \end{aligned} \tag{4}$$

where L is the distance between the source and the first crystal. The position $y''z''$ on the surface of the first crystal is given by the projection of the position $y'z'$ over the surface axes:

$$\begin{aligned} y'' &= y' \frac{\cos(\theta)}{\cos\left(\theta + \frac{\pi}{2} - \theta_C\right)}, \\ z'' &= z' \frac{\cos(\phi)}{\cos(\phi + \delta_1)}. \end{aligned} \tag{5}$$

The angle between the ray and the crystallographic plane of the first crystal is given by

$$\alpha_1 = \arcsin(-\hat{\boldsymbol{e}} \cdot \hat{\boldsymbol{n}}_1), \tag{6}$$

where $\hat{\boldsymbol{e}}$ is the ray vector direction (Eq. (3)) and $\hat{\boldsymbol{n}}_1$ is a unitary vector perpendicular to the crystallographic planes of the first crystal expressed by

$$\begin{aligned} \hat{n}_{1x} &= -\cos(\delta_1)\cos(\theta_C), \\ \hat{n}_{1y} &= \cos(\delta_1)\sin(\theta_C), \\ \hat{n}_{1z} &= \sin(\delta_1). \end{aligned} \tag{7}$$

Therefore, the direction of the reflected ray is given by

$$\hat{\boldsymbol{e}}' = \hat{\boldsymbol{e}} - 2(\hat{\boldsymbol{e}} \cdot \hat{\boldsymbol{n}}_1)\hat{\boldsymbol{n}}_1. \tag{8}$$

If the ray position is within the boundaries of the crystal, a wavelength λ is generated using a Lorentzian random number

generator. The normalized Lorentz function is given by

$$L(\lambda,\lambda_1,\Gamma_1)=\frac{\frac{\Gamma_1}{2\pi}}{(\lambda-\lambda_1)^2+\left(\frac{\Gamma_1}{2}\right)^2}, \tag{9}$$

where λ_1 is the transition wavelength and Γ_1 is the natural line width (FWHM) associated with the decay lifetime. The method used for generating the random number with a Lorentzian distribution is the inverse method (Press et al., 1986). The effect of the Doppler broadening is obtained by generating a wavelength λ' with a Gaussian random number generator centered at the wavelength λ

$$G(\lambda',\lambda,w)=\frac{2}{w}\sqrt{\frac{\ln(2)}{\pi}}\exp\left(-\frac{(\lambda'-\lambda)^2}{\left(\frac{w}{2\sqrt{\ln(2)}}\right)^2}\right), \tag{10}$$

where the FWHM w is given by the velocity distribution of the ions. The Gaussian random number generator is implemented using the Box–Muller method, also based on the inverse method (Press et al., 1986). In that way, we generated a wavelength λ' corresponding to a Voigt profile (the convolution of the Lorentz and Gaussian distributions).

The Bragg angle, θ_B, is related to the wavelength λ' by the well-know relation

$$\lambda'=2d\ \sin(\theta_B), \tag{11}$$

where d is the lattice spacing.

The temperature dependence of the lattice spacing is given by

$$d(T)=d_{22.5}(1+(T-22.5)\eta(T)), \tag{12}$$

where the temperature is given in degree Celsius, $\eta(T)$ is the dilatation coefficient and $d_{22.5}$ is the lattice spacing at $T=22.5$ °C. Since we are dealing with small temperature changes, we neglect the temperature dependence of $\eta(T)$. The quantities $\eta(T)$ and $d_{22.5}$ are deduced form Eq. (1) in Section 2.4.3.

The reflection on the crystals is described by dynamical diffraction theory. The reflectivity curve is created using the Xcrystal component of the XOP 2.3 program (Sanchez del Rio and Dejus, 1998, 2004a) assuming an unpolarized X-ray source, and taking into account the reflections of both σ and π polarizations. Xcrystal implements the dynamical diffraction theory of Zachariasen (1967). This program has an input option for choosing between several input files with form factors obtained from different authors (Chantler, 1995, 2000, 2011; Henke et al., 1993; Kissel, 2000; Waasmaier and Kirfel, 1995). The reflectivity curves are shown in Fig. 12 for a monochromatic line at an energy of 3104 eV. In the simulation program the reflectivity curve is interpolated using cubic splines and used as a probability distribution for the reflection of an X-ray.

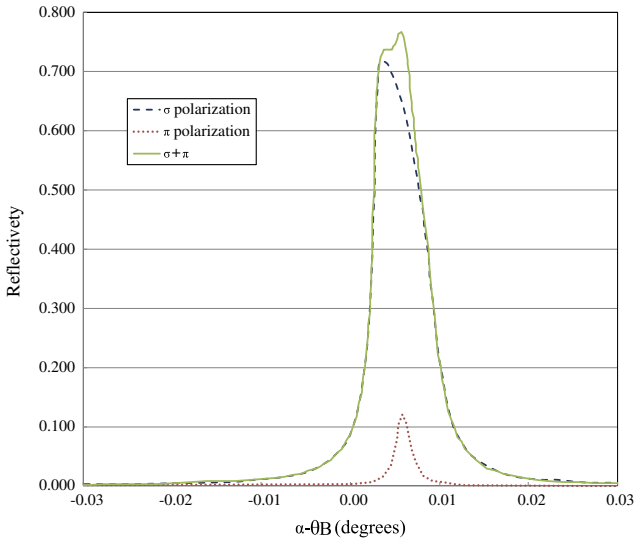

Fig. 12. Si(111) reflectivity curve (diffraction profile) for σ (blue dashed) and π (red dotted) polarizations as well as their sum (green full), evaluated with Xcrystal, a component of XOP. α is the angle between the X-ray and the crystallographic plane given by Eq. (6). (For interpretation of the references to color in this figure caption, the reader is referred to the web version of this paper.)

The reflectivity curve is evaluated at the Bragg angle corresponding to the wavelength λ' (Eq. (11)) and at the angle α_1 (Eq. (6)). The curve depends on the index of refraction and absorption coefficients, which are energy-dependent. In the region of energy where we have performed the measurements (3096–3139 eV) the FWHM of the reflectivity curve changes by 0.08%/eV and the peak reflectivity by 0.1%/eV. The same diffraction profile is used for each wavelength of an X-ray line distribution, since the variation of the diffraction profiles within the range of the peak is negligible (the typical widths of our lines are a few hundreds of meV FWHM).

The simulation program is also designed to take into account a small mosaicity of the crystal. A Gaussian distribution for the orientation of the crystal surface (θ_C) is used. When comparing experimental and simulated line profiles, we notice that this effect is very small and can be neglected. This is consistent with the fact that the crystals had a special surface treatment as described in Section 2.4. We also neglect the variation of the crystal lattice spacing as a function of position as it is measured to be small as explained in Section 2.4.

Once the ray is reflected, the y_a position along the $x_a y_a z_a$ axis is given by $y_a=-y''\ \sin(\theta_T-\theta_C)$. The direction vector obtained from Eq. (8) is given in this axis by multiplying it by a rotation matrix along the z-axis with angle θ_T. The position vector at the second crystal in the non-dispersive or dispersive setup is obtained in the same way as for the first crystal with a translation given by Eq. (4) with L being the distance between the crystals and a projection over the surface of the second crystal. Similar to Eq. (5), the position at the second crystal crystallographic plane obtained after projection is given by

$$y''_a=y'_a\frac{\cos(\theta)}{\cos(\pm\theta+\theta_C\mp\beta)},$$
$$z''_a=z'_a\frac{\cos(\phi)}{\cos(\phi+\delta_2)}, \tag{13}$$

where the plus and minus signs refer to the dispersive and non-dispersive modes, respectively. As in the case of the first crystal, if the ray position is inside the area of the second crystal, then the glancing angle between the ray direction and the second crystal surface (α_2) is calculated to evaluate the reflectivity. Furthermore, similar to the first crystal evaluation part, the glancing angle is obtained from Eq. (6) with $\hat{\boldsymbol{e}}_a$ defined after the first crystal reflection (Eq. (8)) and the normal vector of the second crystal $\hat{\boldsymbol{n}}_2^{\pm}$ is given by

$$\hat{n}_{2x}^{\pm}=\mp\cos(\delta_2)\sin(\theta_T\pm\theta_C+\beta),$$
$$\hat{n}_{2y}^{\pm}=\pm\cos(\delta_2)\cos(\theta_T\pm\theta_C+\beta),$$
$$\hat{n}_{2z}^{\pm}=\sin(\delta_2).$$

The direction vector of the ray reflected from the second crystal is given in the $x_b y_b z_b$ coordinate system by multiplying it by a rotation matrix along the z-axis with an angle $\theta_T+\theta_D^{\pm}$, where $\theta_D^{\pm}$ is the angle between the detector in the dispersive or non-dispersive modes and the axis of the source. Finally, the position of the ray at the detector entrance plane in both modes is obtained from Eq. (4) with L being the distance between the second crystal

and the detector. If the ray reaches the detector, then a count is added to the simulated spectrum for the value of β.

4. Data analysis

In previous work, the method used to deduce the energy from experiment was to fit the experimental spectrum with a Voigt profile to obtain the angle position of the peak and apply the Bragg law with index of refraction and vertical divergence corrections. The problem is that the crystal reflection curve is asymmetric (Fig. 12). In non-dispersive mode, the asymmetry disappears because the rocking curve is the convolution of the profile of Fig. 12 with its mirror image. Fig. 13 shows an experimental non-dispersive spectrum fitted with a Voigt profile and with a sequence of simulations, corresponding to different Gaussian broadenings of the X-ray line. It shows clearly that within the statistical uncertainty of the simulated profile the fit quality is the same as with a Voigt profile. In addition, Fig. 13 clearly demonstrates the high level of agreement between the simulation and the experimental profile. We would like to emphasize that, except for the energy used in the simulation, there is no adjustable parameter here. Moreover, since it is a non-dispersive profile, the intrinsic width of the line does not change the shape as expected. In the dispersive side, the reflection curve is convolved with itself, which enhances the asymmetry. An example of a fit by a Voigt and fits by a sequence of simulated profiles is shown in Fig. 14, where we represent a profile in the dispersive configuration. The peak corresponds to the $1s2s\ ^3S_1 \rightarrow 1s^2\ ^1S_0$ M1 transition energy in Ar^{16+}. Again, for the profile with the width that provides the smaller χ^2, the fit quality is excellent, and the reduced χ^2 very close to 1, showing the quality of the simulation. The asymmetry of the line translates into a difference of 1.86×10^{-3} degrees between the peak positions obtained from the simulation and the Voigt fit, while it is only 1.3×10^{-4} degrees in the non-dispersive side. In the dispersive side, it corresponds to 19 times the angular encoder error. Moreover, because of the complicated line shape, the value of the angle corresponding to the peak position of the simulated profile itself is not a well defined quantity. The only well defined quantity is the energy of the line that has been used in the simulation. We thus used two independent methods to analyze the experimental data and check our results. In the first one, we used an analytic approximation of the asymmetric profile. This can be used to fit experimental profiles and establish a direct relationship between the energy and the peak position, since the asymmetry is already included in the model (Amaro, 2011). In the second one, we fitted both the simulated and the experimental non-dispersive profiles, as well as dispersive profiles with a Voigt profile. The angular difference between the resulting dispersive and non-dispersive peak positions is related to the uncorrected Bragg angle ($\theta = 180 - (\theta_{\mathrm{dis}} - \theta_{\mathrm{nondis}})/2$).

Using this angle, the line energy is

$$E(T,\theta) = \frac{Cn}{2d(1+\alpha(T-T_0))} \times \frac{1}{\sin(\theta+\chi\ \tan\ \theta)\ \ 1-\frac{\delta}{(\sin\ \theta)^2}\Big)} \tag{14}$$

where n is the order of diffraction, δ is the index of refraction, $C = hc$ is the wavelength to energy conversion factor equal to 12,398.41875(31) eV Å (Mohr et al., 2008). The coefficient χ is the

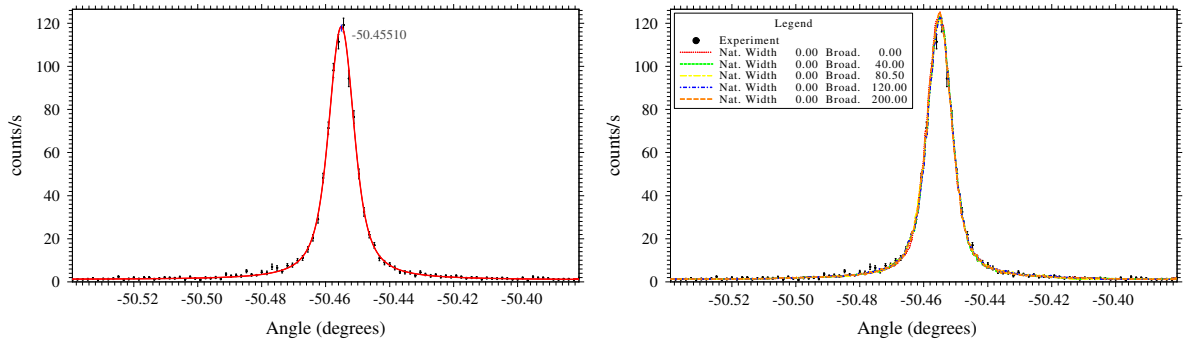

Fig. 13. Raw measurement data in the non-dispersive mode as a function of the second crystal diffraction angle fitted by a Voigt profile (left) and by simulated profiles with different line widths (right). The Voigt profile fit yields $\chi^2 = 1.12$ while the simulated ones give χ^2 ranging from 1.2 to 1.4 (the variation is mostly due to the statistics of the simulated profiles). The angle difference value between fitting with Voigt function and with simulations is equal to 1.3×10^{-4} degrees. The spectrum represents an experimental non-dispersive rocking curve for the crystals at the X-ray energy of the $1s2s\ ^3S_1 \rightarrow 1s^2\ ^1S_0$ M1 transition in Ar^{16+} (theoretical value: 3104.148 eV see text).

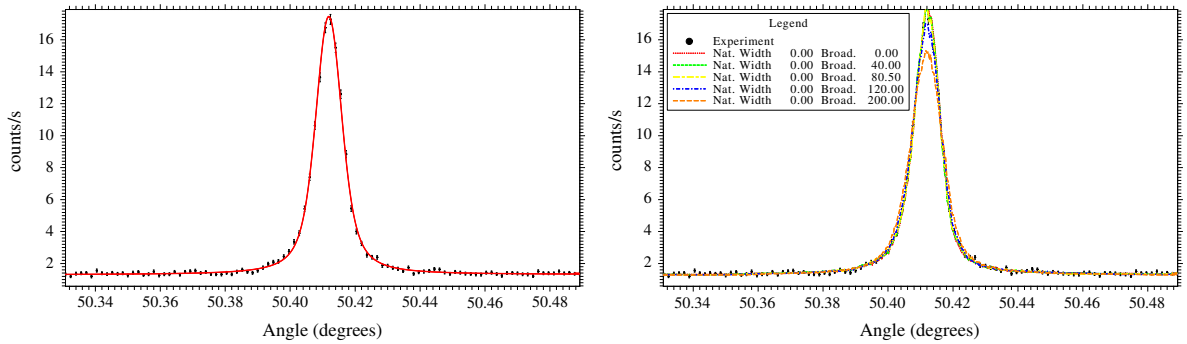

Fig. 14. An experimental dispersive mode spectrum of the $1s2s\ ^3S_1 \rightarrow 1s^2\ ^1S_0$ transition in Ar^{16+} as a function of the second crystal angle fitted by a Voigt profile (left) and simulated profiles with different line widths (right). The Voigt profile fit yields a $\chi^2 = 1.42$ and the optimum simulated profile fit (for a Gaussian broadening of 80 meV) gives $\chi^2 = 1.26$. The angle difference value between the peak positions obtained with the two fits equals to $1.86(7) \times 10^{-3}$ degrees.

vertical divergence correction (Bearden and Thomsen, 1971):

$$\chi = \frac{a^2+b^2}{24L^2}, \tag{15}$$

where a and b are the heights of the slits which define the height of the X-ray beam (in our case the polarization electrode and the detector window), and L is the distance between these slits. The difference in angle $\delta\theta = \theta_s - \theta_e$ and in temperature $\delta T = T_s - T_e$ between simulation and experimental cases are then used to correct the energy used in the simulation. The final energy E_f is written in term of the simulation energy E_s as

$$E_f = E_s + \frac{\partial E(T,\theta)}{\partial T}\delta T + \frac{\partial E(T,\theta)}{\partial \theta}\delta\theta. \tag{16}$$

This method takes into account the asymmetric profile because for a given input E_s in the simulation, the value θ_s is known. Both independent methods provide the same result with high accuracy giving confidence that the asymmetry in the dispersive profile is properly taken into account.

The fit program uses the least-square method, with the Levenberg–Marquardt algorithm, in the implementation of Press et al. (1986).

The Voigt profile is a convolution product of a Lorentzian (representing the emission profile of the line) and of a Gaussian (representing an instrumental broadening), see, e.g., Armstrong (1967). It is written as

$$I(\theta,\theta_0,\ell,g) = I_0\frac{K(x,y)}{K(0,y)} \tag{17}$$

with the reduced Voigt function

$$K(x,y) = \frac{y}{\pi}\int_{-\infty}^{\infty} dt \frac{e^{-t^2}}{(t-x)^2+y^2} \tag{18}$$

$$x = \frac{2(\theta-\theta_0)\sqrt{\ln 2}}{g} \tag{19}$$

$$y = \frac{\ell}{g}\sqrt{\ln 2}, \tag{20}$$

where θ_0 is the peak position, I_0 the intensity at θ_0, ℓ the Lorentzian FWHM and g the Gaussian FWHM. The FWMH of the Voigt profile can be given to a very good approximation as

$$w = \frac{\ell + \sqrt{\ell^2+4g^2}}{2}. \tag{21}$$

An exact expression was derived by Jian and Qingguo (2007, Eq. (21)). It provides values in an excellent agreement with the previous equation, but is much less convenient to use. The Voigt profile and the needed derivatives are evaluated following the method described in Armstrong (1967) and Indelicato (1983).

5. Study of uncertainties

The systematic errors in the measurement performed using the spectrometer described here can be divided into three categories. The first one includes the uncertainties due to the alignment and to the precision of the construction of the DCS. The second one is related to uncertainties in the knowledge of the diffraction profiles and on the polarization of the X-rays. The third category is due to the uncertainty of the knowledge of fundamental constants or crystal properties like the lattice spacing. Uncertainties from the first two categories can be estimated with the help of the simulation program described in Section 3. The energy deduced from simulated spectra is evaluated following the method described in Section 4. By comparing the energy values obtained in simulations for several values of a given parameter (ideal case included), we get an estimation of that parameter contribution to the uncertainty. We give in Table 2 the list of contributions to the final error budget for the absolute measurement of the He-like Ar $1s2s\ ^3S_1 \rightarrow 1s^2\ ^1S_0$ M1 transition. All simulations were performed with an input energy of 3104.148 eV, which is the theoretical value of that transition (Artemyev et al., 2005). Most contributions to the uncertainty change very slowly with energy. The different contributions are explained below.

5.1. Geometrical uncertainties

Two of the geometrical uncertainties are related to the alignment. The uncertainty in the verticality of the crystal diffracting planes is due to the alignment procedure described in Section 2.3 and to the error in the cut angle of the crystal (Section 2.4). To this uncertainty, one has to add the one due to a possible misalignment of the DCS input collimators (Fig. 15). The total effect of these misalignments can be checked by recording X-ray spectra with absorbing masks that cover alternatively the upper and lower halves of the crystals. The comparison of the energies obtained in the two measurements gives an indication of the total uncertainty on the alignment within the statistical uncertainty of the measurement. Fig. 16 shows the simulated energy difference obtained with upper and lower mask positions for several values of crystal tilts, $\delta_{1,2}$. Similarly, Fig. 17 shows the energy difference between the upper and lower mask cases for several values of vertical shifts of the lead collimator (see Fig. 15 b) that connects the source to the spectrometer.

As explained in Section 2.3, the alignment procedure provides $\delta_i \leq 0.01^\circ$. The uncertainty related to crystal tilts was obtained from the simulation program, comparing energies from simulations using $\delta_i = 0, \pm 0.01^\circ$. This uncertainty is in good agreement with the expressions of Bearden and Thomsen (1971).

The uncertainty related to the vertical misalignment of collimators was obtained in a similar way by running simulations with a collimator entrance shifted by $\pm$ 0.45 mm (see Fig. 15 a and b), i.e., with a vertical shift of the collimator so that $(\phi_{max}+\phi_{min})/2 = \pm 0.01^\circ$ (the total spectrometer length is 2.6 m). The relevant dimensions are given in Fig. 2. The equivalent situation for a vertical shift in the detector position is

Table 2
List of uncertainties and error contributions. The simulations were performed for an X-ray energy of 3104.148 eV, which corresponds to the $1s2s\ ^3S_1 \rightarrow 1s^2\ ^1S_0$ transition in He-like argon. The uncertainty due to form factors was obtained by comparing simulations with different form factor values from Refs. Chantler (1995, 2000, 2011), Henke et al. (1993), Kissel (2000), and Waasmaier and Kirfel (1995). The X-ray polarization uncertainty is obtained by comparing a simulation done with a crystal reflection profile for a fully σ-polarized and an unpolarized beam.

Contribution	Value (eV)
Geometrical uncertainties	
Crystal tilts ($\pm 0.01^\circ$ for each crystal)	0.0002
Vertical misalignment of collimators (1 mm)	0.0002
X-ray source size (6–12 mm)	0.0013
Diffraction profile uncertainties	
Form factors	0.0020
X-ray polarization	0.0014
Instrumental limitations and uncertainties on physical constants	
Fit and extrapolation to standard temperature	0.0044
Angle encoder error (0.2 arc s)	0.0036
Lattice spacing error	0.0001
Index of refraction	0.0016
Coefficient of thermal expansion	0.0002
Temperature (0.5 °C)	0.0040
Energy—wavelength correction	0.0001
Total	0.0077

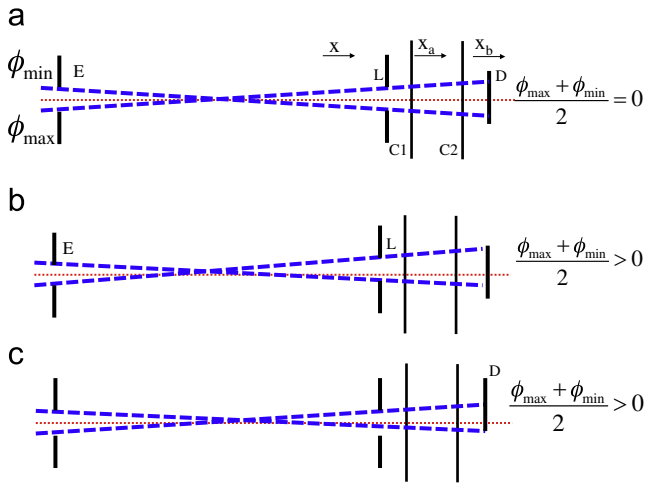

Fig. 15. Scheme of the collimator system. The points E and L refer to the entrance of the X-rays and to the lead collimator respectively, as represented in Fig. 2. C1, C2 and D represent the first and the second crystal and the detector, respectively. (a) represents an ideal alignment; (b) a vertical misalignment of L compared to E; (c) a vertical misalignment of the detector. The dashed lines represent rays with either maximum or minimum vertical divergence ϕ. The dotted line is the symmetry axis. (a) Ideal alignment, (b) Collimators misaligned and (c) Detector misaligned.

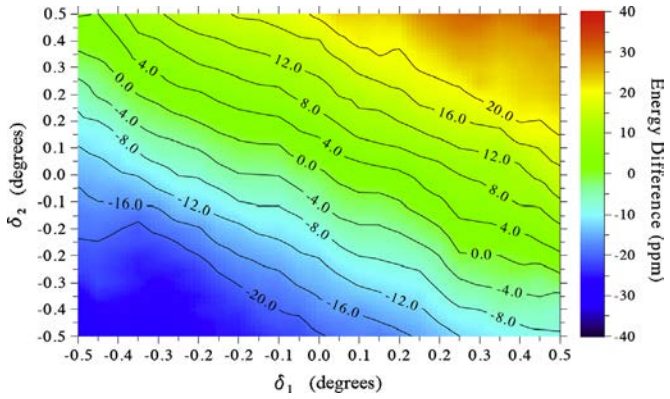

Fig. 16. Plot of the energy difference (ppm) between upper and lower masks used on the second crystal for several values of crystal tilts of δ_1 and δ_2. The simulations were performed for an X-ray energy of 3104.148 eV, which corresponds to the $1s2s\ ^3S_1 \rightarrow 1s^2\ ^1S_0$ transition in He-like argon.

represented in Fig. 15(c). From a geometrical point of view, it is irrelevant which elements are restricting ϕ_{max} and ϕ_{min}. We thus performed a single simulation, shifting the input collimator by $\pm$ 1 mm, leading to a large overestimate of the total uncertainty.

Previous measurements with a DCS used high-power X-ray tubes to provide X-ray lines from solid targets or sometimes gas targets (Mooney et al., 1992). Here we use a plasma, the geometry and position of which are fixed by the magnetic field configuration, the microwave frequency and power, and possibly other factors like ionic and electronic temperatures and polarization electrode bias. The plasma, as fixed by the magnetic field structure, is $\approx$30 mm in diameter. Yet, X-ray imaging was performed before on an ECRIS (Biri et al., 2004), which shows that the HCI position with respect to the source axis may change depending on the operating conditions. To estimate possible uncertainties due to this effect, we performed two simulations for an X-ray plasma diameter of 12 mm (diameter of the collimator) and another for a 6 mm plasma diameter. We find a difference of 1.3 meV, which we use as a largely overestimated uncertainty in Table 2.

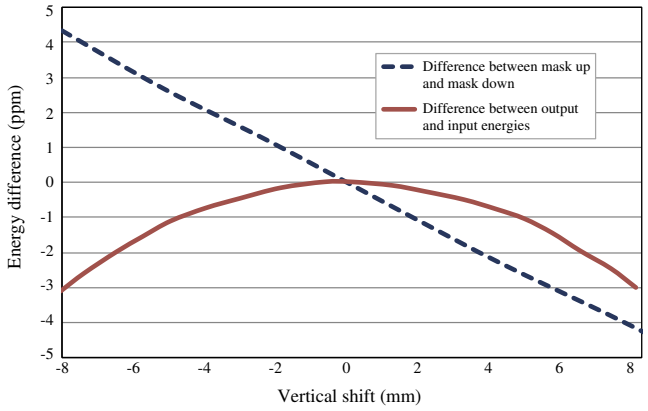

Fig. 17. Energy difference (ppm) between configurations with an upper or lower mask for several values of a vertical shift in the position of the spectrometer's collimator. The solid line is the difference between the input and output energies of the simulation. The dashed line is the difference between the simulation energy outputs for the upper and lower masks. The simulations were performed for an X-ray energy of 3104.148 eV, which corresponds to the $1s2s\ ^3S_1 \rightarrow 1s^2\ ^1S_0$ transition in He-like argon.

Besides vertical and horizontal angle shifts, we considered also the case of the uncertainty due to a possible vertical or horizontal translation of the crystals. No observable difference was noticed in the simulated results.

Another possible uncertainty source could be due to a small crystal curvature. Simulations performed for this effect show that the non-dispersive profile is the most sensitive to curvature. The variations of the width of the dispersive and non-dispersive profiles as a function of the radius of curvature are shown in Fig. 18. Changes in the dispersive-side width are small, at the limit of the statistical significance. Changes in the non-dispersive side are large for radii of curvature smaller than 1000 m. The crystal curvature also induces a dependence of the non-dispersive spectra width on the first crystal angle. Fig. 19 shows a plot of the non-dispersive width for several values of the first crystal angle. The black line represents the value obtained for a curvature radius larger than 1000 m, while the red dots were obtained using a radius of 400 m. This figure shows clearly a dependence of the width on the first crystal angle that can be checked experimentally. Finally the dependence of the line energy on the radius of curvature is plotted in Fig. 20. The figure shows that for radii of curvature larger than 5000 m, the shift is much smaller than the statistical error on the fit. This effect is experimentally minimized by using thick crystals (6 mm) and nylon screws just brought to contact, to hold the crystal against the reference surface of the support as described in Section 2.2. We were able to see experimental evidence of crystal bending when pressing them hard against their supports with strongly tightened brass screws. We were then able to observe experimentally a broadened line profile in the non-dispersive mode, corresponding to a bending radius of $\approx$ 500 m and a dependence of the width on the first crystal angle as reported in Fig. 19. This effect disappeared completely (as seen in Fig. 24 of Section 6) with the normal mode of holding the crystals, and the parallel profiles show no signs of broadening as seen in Fig. 13.

5.2. *Diffraction profile uncertainties*

The energy values obtained with a DCS in reflection at low energy depend critically on the quality of the crystal reflectivity curve. The peak position is dependent on the index of refraction, for which very few experimental determinations exist, all obtained at high energy. As described in Section 3, we use two programs, XOP (Sanchez del Rio and Dejus, 2004a,b, 1998) and X0h, (Lugovskaya and Stepanov, 1991, Stepanov) to calculate reflectivity curves in the simulations. Moreover, we use the capacity of XOP to choose different form factor values (Chantler, 1995, 2000, 2011; Henke

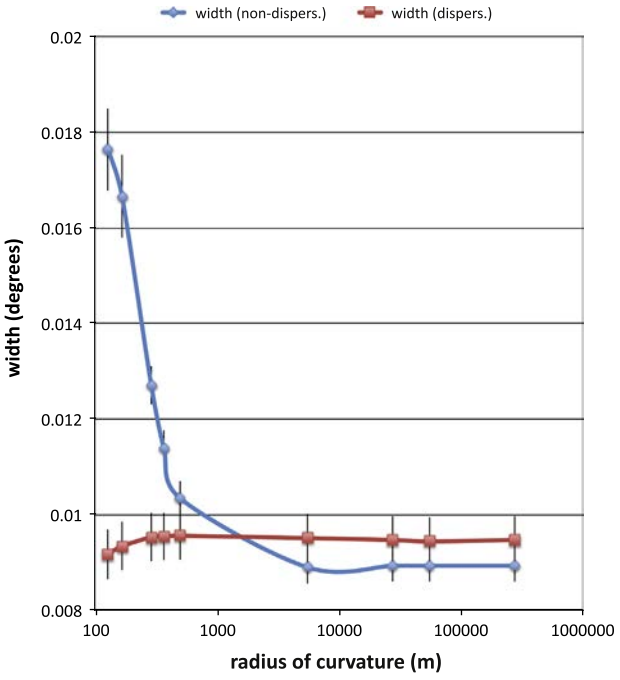

Fig. 18. Widths of the dispersive and non-dispersive profiles as a function of the crystals radius of curvature. These widths are obtained by fitting simulated spectra with a Voigt profile and combining the Lorentzian and Gaussian widths using Eq. (21). Error bars are due to statistics. The dispersive and non-dispersive widths are identical for large radii of curvature as expected, within simulation statistical uncertainty.

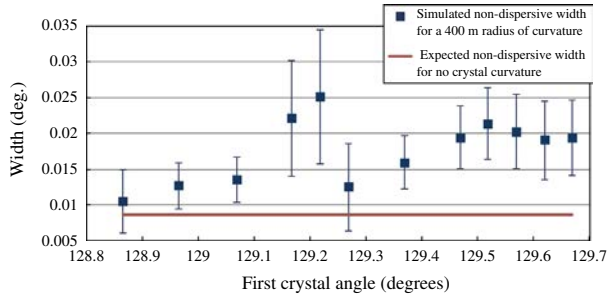

Fig. 19. Simulated, non-dispersive width, plotted for several values of the first crystal angle and a crystal curvature radius of 400 m in both crystals (blue squares), or no curvature (solid red line), for the He-like Ar M1 line. (For interpretation of the references to color in this figure caption, the reader is referred to the web version of this paper.)

et al., 1993; Kissel, 2000; Waasmaier and Kirfel, 1995). By comparing simulations performed with the diffraction curves from the two different programs and with the different form factors, we obtain an uncertainty of 2 meV for the diffraction profile.

The index of refraction provided by XOP is 5.1005×10^{-5} for a line energy of 3104.148 eV. Henke et al. (1993) provide the semi-empirical value of 5.0790×10^{-5}, and Brennan and Cowan (1992) the value of 5.0825×10^{-5}. The maximum variation of the final energy using the different values of the index of refraction in Eq. (14) is 1.6 meV, which we use as an uncertainty for this parameter.

The uncertainty due to unknown *polarization* of the X-rays was also estimated with the use of simulations. We performed two simulations; one with a diffraction profile containing only the σ polarization and another with $\sigma+\pi$ polarization (unpolarized). From the difference a maximum uncertainty of 1.4 meV can be estimated due to the presence of any polarized light. The integrated reflectivity using only π polarization is 6% of the one obtained with σ polarization. This

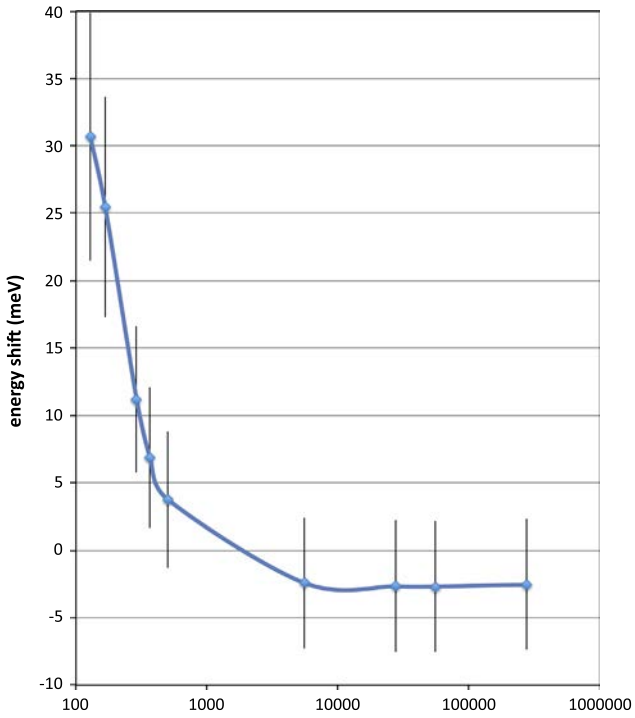

Fig. 20. Energy shift due to a curvature of the two crystals. These shifts are obtained by fitting simulated spectra with a Voigt profile. Error bars are statistical error bars.

would lead to roughly 230 times fewer counts. The width of the profile obtained using only π polarized X-rays is roughly 30% smaller than the width of a profile obtained with the σ polarization. The agreement between experimental profile widths and simulation widths performed for unpolarized X-rays is excellent. This confirms within the statistical uncertainty in the experimental spectra that the X-ray beam from the ECRIS is not polarized and justify the uncertainty we quote in Table 2.

We also considered other effects like distortion of the reflectivity due to *pendellösung*. These effects are significant only in crystals with small thicknesses, which is not the case of the crystals used in this work. For example, for the energy of 3104.148 eV we noticed (using both XOP and X0h) that these effects are completely washed out in crystals with thicknesses greater than 20 μm, and the crystals we used have a thickness of 6 mm.

The penetration depth of 3.1 keV X-rays in Si is very small. We get 1.44 μm for σ-polarization with XOP. This corresponds to an extinction length of 2.26 μm. For the π-polarization they are 7.6 μm and 12 μm, but we have seen that this polarization contributes only a small fraction to the profile. We take into account the fact that each ray is reflected at a different depth in the crystal in the simulation. An exponential distribution with a mean value equal to the *penetration depth* is used to obtain the depth where the ray is reflected. Simulations show that it would require penetration depths of a few mm to change significantly the measured energy. This effect can thus be completely neglected.

The effect of a small *mosaicity* of the crystals was also considered as a source for possible broadening of the diffraction profiles. Simulations show that non-negligible uncertainties due to this effect can only happen for values of mosaicity that produce a much larger width of the simulated non-dispersive profiles than the ones observed in the experiment.

The method of alignment of the crystals for polishing gives rise to an *asymmetric cut* uncertainty of ≈ 10 arc s (Section 2.4.1). We

used XOP to estimate a possible broadening of the diffraction profile due to this and no difference was observed. Furthermore, we simulated the effect of an asymmetric cut of that size on the energy and found none. This uncertainty was checked experimentally by turning the crystal upside down between two measurements and by comparing the non-dispersive profiles. With the experimental statistics reachable in the current setup, we did not observe any difference in the diffraction profiles with flipped crystals. This gives us confidence on the present uncertainty due to the asymmetric cut of the crystals.

5.3. Other sources of uncertainty

As can be seen from Table 2, the largest source of uncertainty comes from the statistical uncertainty of the fit, and from the extrapolation of data taken at different temperatures to the standard temperature (22.5 °C). To this must be added uncertainties on fundamental constants and crystal physical properties.

The main source of uncertainty lies in the difficulty of stabilizing the crystal temperatures under vacuum, with the stepping motors heating the crystal supports and the ECRIS klystron heating the room. The temperature controller is perfectly able to maintain a very stable temperature at atmospheric pressure, but not under vacuum. The use of special graphite contact sheets to improve the contact between the thermistors and the crystal could not completely fix the problem. Most of the time, it was not possible to set the temperature to below 22.7 °C. In order to alleviate this difficulty, we perform sequences of measurements at various temperatures and extrapolate to 22.5 °C. This problem leads then to two different uncertainties: one is due to the precision of the temperature measurement, which we assume to be much worse than the calibration of the thermistors. The second is due to the extrapolation procedure, which combines the statistical uncertainty of the peak position determination and the one due to the fit of a linear function to the temperature dependance of the peak positions and extrapolation to standard temperature. This problem will be fixed in the next version of the crystal supports, using IR sensors, which will directly measure the IR radiation from the crystals. The thermistors will no longer need to be attached to the crystals, but will be mechanically attached to the copper backing.

The next large source of uncertainty is related to the precision of the angular encoders. With a Si(111) crystal, and a Bragg angle of $\approx 39°$, the dispersion is such that a 0.2 arc s accuracy in angle measurement leads to an uncertainty of 3.6 meV or 1.2 ppm. This would get worse for X-rays of heavier elements, giving 1.4 ppm for the M1 transition in He-like K (3.47 keV), 1.6 ppm for the M1 transition in He-like Ca (3.86 keV) and 3.1 ppm for He-like Fe (6.64 keV). Using Si (220) leads to a very small 0.4 ppm uncertainty in the Bragg angle for the M1 transition in He-like potassium. One can obtain 1.7 ppm for Fe in the first order and 0.2 ppm in the second order. That measurement would require a very bright X-ray source. One could go beyond this limitation by doing a careful calibration of the encoder using a photoelectronic autocollimator (Luther et al., 1984) and a 24-sided optical polygon as has been done at NIST (Mooney et al., 1992; Schweppe et al., 1994).

The last large uncertainty in this category is related to the fact that there are no accurate measurements of the index of refraction of Si at these energies. There has been a proposition to do it by comparing directly the deflection angle in transmission and reflection, but it has not been implemented (Hudson, 2000). Such a measurement, if accurate could validate the theoretical or semi-empirical values (Henke et al., 1993) (which uses atomic experimental and theoretical photoabsorption cross sections) that we have used and reduce the uncertainty.

6. Results and discussion

In Figs. 13 and 14 we present a measurement of the non-dispersive and dispersive spectra obtained with the DCS for the relativistic M1 transition $1s2s\ ^3S_1 \rightarrow 1s^2\ ^1S_0$ in Ar^{16+}. The data were acquired by summing individual back-and-forth 100 bins scans, lasting roughly 10 min in the non-dispersive case and 20 min in the dispersive case. The non-dispersive spectrum was acquired in 943 s and the dispersive one in 18,240 s (these values are corrected for dead time, corresponding to periods when the first crystal position has drifted and is being corrected). In Fig. 21 we show a survey spectrum, in which the angular range was chosen to include peaks corresponding to transition energies of Ar^{14+}, Ar^{15+} and Ar^{16+} ions. The tallest peak on the left side corresponds to the transition $1s^22s^22p\ ^1P_1 \rightarrow 1s^22s^2\ ^1S_0$ in Ar^{14+}. Next to this peak is a small peak corresponding to a blend of the $1s2s2p^2\ ^1S_0 \rightarrow\ 1s^22s2p\ ^1P_1$ transition also in Ar^{14+} and to the $1s2s2p^3\ ^2D^{(2)}_{3/2} \rightarrow\ 1s^22s2p^2\ ^4P_{5/2}$ and $1s2s2p^3\ ^2P^{(1)}_{1/2} \rightarrow 1s^22s2p^2\ ^4P_{1/2}$ transitions in Ar^{13+}. The transition in Ar^{14+} has a strong fluorescence yield, but a 1 eV energy shift. The two transitions in Ar^{13+} have a low fluorescence yield (a few 10^{-5}), but one has the right shift compared to the large peak (1.6 eV) and the Ar^{13+} charge state is more abundant than Ar^{14+}. The central peak is the M1 transition in Ar^{16+}. The double peak on the right corresponds to the doublet $1s2s2p\ ^2P_{1/2,3/2} \rightarrow 1s^22s\ ^2S_{1/2}$ in Ar^{15+}. A description of the mechanism leading to this spectrum can be found in Costa et al. (2001), Martins et al. (2001, 2009), and Santos et al. (2010, 2008, 2011). Spectra like the one in Fig. 21 allowed us to measure the charge distribution in the ECRIT (Guerra et al., 2013).

The magnetic dipole (M1) transition has a natural width several orders of magnitude smaller than any line ever measured with a DCS until now. Its measured dispersive width is close to the non-dispersive peak width, which represents the intrinsic response function of the instrument. The continuous lines in Figs. 13 and 14 (right) correspond to simulated profiles fitted to the measured spectra. These simulated profiles were evaluated for the case of an aligned DCS, unpolarized X-rays and a diffraction profile of an ideal flat crystal, with a negligible mosaicity and asymmetric cut. The simulation reproduces the non-dispersive data with a reduced $\chi^2 \approx 1.2$. This precise fit of the simulated profile on the experimental spectra with no adjustable parameters except line position and intensity validates the hypothesis of perfect crystals and of an ideal alignment of the spectrometer components as made in the simulation. On the dispersive side, we fitted using simulations

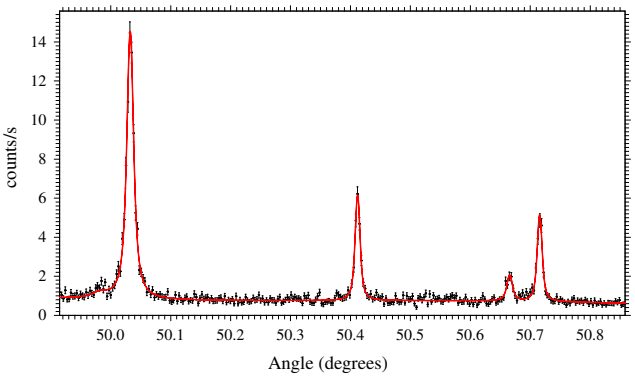

Fig. 21. Experimental survey dispersive spectrum. The small leftmost peak is a combination of the $1s2s2p^2\ ^1S_0 \rightarrow 1s^22s2p\ ^1P_1$ transition in Ar^{14+} and of the $1s2s2p^3\ ^2D^{(2)}_{3/2} \rightarrow 1s^22s2p^2\ ^4P_{5/2}$ and $1s2s2p^3\ ^2P^{(1)}_{1/2} \rightarrow 1s^22s2p^2\ ^4P_{1/2}$ transitions in Ar^{13+}. Large left peak: $1s2s^22p\ ^1P_1 \rightarrow 1s^22s^2\ ^1S_0$ in Ar^{14+}, central peak: $1s2s\ ^3S_1 \rightarrow 1s^2\ ^1S_0$ in Ar^{16+}, right peaks: $1s2s2p\ ^2P_{1/2,3/2} \rightarrow 1s^22s\ ^2S_{1/2}$ in Ar^{15+}. The line represents a fit using a sum of Voigt profiles.

with various values of the Gaussian width representing the Doppler broadening due to the ion motion in the ECRIS. The dependance of the χ^2 on the width corresponding to the spectrum of Fig. 14 is plotted in Fig. 22. The minimum corresponds to a width of 77.6(6.7) meV and to a reduced $\chi^2 = 0.75$.

In Section 3 we discussed a method for probing vertical alignment errors using crystal masking. We used this method, performing several measurements using the Be-like line (the most intense peak in Fig. 21) with a first crystal angle of 130°. In the first set of measurements, we have placed a thick brass mask on the upper half of the second crystal. In the second set of measurements, the lower half of the second crystal was blocked with the same mask.

Fig. 23 shows the line energies obtained by analyzing all the measurements performed with both mask positions. A first set of measurements was performed in April 2010, while the second set of measurements was done in March 2011. The energy obtained in the analysis using Voigt profiles for mask covering the upper half is 3091.780 ± 0.005 eV. For a mask covering the lower half of the crystal, it is 3091.777 ± 0.005 eV, corresponding to an energy shift of 3 ± 7 meV. The uncertainty is only due to statistics. The observed shift is consistent with the one expected from the alignment uncertainty, which is 1.5 meV for 0.01° as can be seen from Fig. 17.

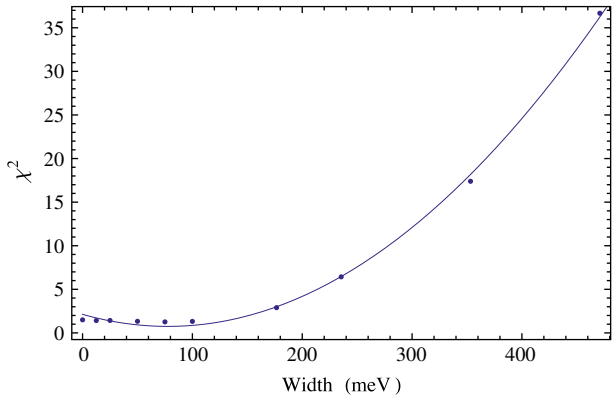

Fig. 22. Variation of the χ^2 as a function of the Gaussian width introduced in the simulation to represent the Doppler broadening corresponding to the ions temperature.

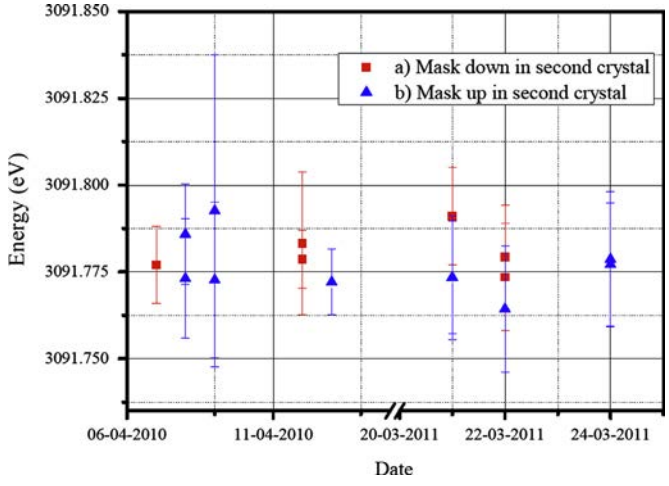

Fig. 23. Plot of the energy obtained for the mask test. The red squares (a) correspond to the mask placed on the lower half of the second crystal in the DCS. The blue triangles (b) show measurement results for the mask placed on the upper half of the second crystal. (For interpretation of the references to color in this figure caption, the reader is referred to the web version of this paper.)

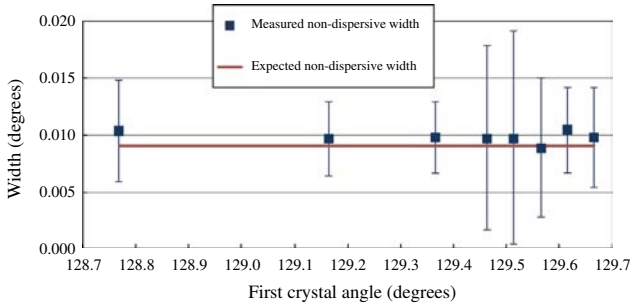

Fig. 24. Measurements of the non-dispersive width for several values of first crystal angle.

We also experimentally checked the curvature of both crystals, to verify if it can be neglected. We thus performed measurements of the non-dispersive width for several values of the first crystal angle as plotted in Fig. 24. Comparing Figs. 19 and 24 we notice that there is no observable dependence of the width on the first crystal angle within the statistical uncertainty. Furthermore, the non-dispersive width is the same as the one expected from a plane crystal. This fact gives us confidence that the crystal holding method does not produce a curvature in the crystals.

7. Conclusions

We provide a complete description of an experimental setup composed of a double crystal spectrometer and of an electron-cyclotron resonance ion source, designed to measure low energy X-rays from middle-*Z* highly charged ions on an absolute energy scale. We experimentally demonstrated that the ECRIS plasma yields the necessary X-ray intensity to perform accurate measurements with a DCS. An *ab initio* simulation of the experimental setup (based on the spectrometer and the source geometry) is presented. The simulations describe very accurately experimental line shapes without adjustable parameters. We show by a complete sequence of measurements and simulations that we understand the systematic errors within the present statistical accuracy of the experimental spectra. The spectra presented in this work clearly show that even a relatively small, permanent magnet ECRIS provides high enough intensities for precision measurements of transitions in highly charged ions with a DCS. We also show that our understanding of the line shape is such that we can investigate the ion temperatures in the plasma. We are thus now able to obtain values of the natural line widths in ions with 2, 3 or 4 electrons, leading to a better understanding of the Auger and radiative contributions to the width.

The world-wide unique combination of the DCS and the ECRIS allows measurements of high-precision, reference-free X-ray transition energies in highly charged ions. These high precision measurements enable direct tests of QED and many-body effects in middle-*Z* elements and will provide new X-ray standards based on narrow transitions of highly charged ions. A 2.5 ppm (Table 2) measurement of the $1s2s\ ^3S_1 \rightarrow 1s^2\ ^1S_0$ transition energy in Ar^{16+} obtained with this setup has been published recently (Amaro et al., 2012) and preliminary results for the energy and the width of the $1s2p\ ^1P_1 \rightarrow 1s^2\ ^1S_0$ transition in Ar^{16+} and the $1s2s^2\ 2p\ ^1P_1 \rightarrow 1s^2 2s^2\ ^1S_0$ transition in Ar^{14+} can be found in Szabo et al. (2013).

Acknowledgments

Laboratoire Kastler Brossel is “UMR n° 8552” of the ENS, CNRS and UPMC. The SIMPA ECRIS has been financed by Grants from

CNRS, MESR, and UPMC. The experiment is supported by Grants from BNM *01 3 0002*, the ANR *ANR-06-BLAN-0223* and the Helmholtz Alliance *HA216/EMMI*.

This research was also supported in part by FCT-Fundação para a Ciência e Tecnologia (Portugal) through Project nos. PEst-OE/FIS/UI0303/2011 and PTDC/FIS/117606/2012, by the French-Portuguese collaboration (PESSOA Program, Contract no. 441.00), by the Acções Integradas Luso-Francesas (Contract no. F-11/09), and by the Programme Hubert Curien PESSOA 20022VB. M. G. acknowledges the support of the FCT, under Contract SFRH/BD/38691/2007. P. A. acknowledges the support of FCT, under Contract no. SFRH/BD/37404/2007 and the German Research Foundation (DFG) within the Emmy Noether program under Contract no. TA 740 1-1. We thank J. P. Okpisz, B. Delamour, M. Boujrad, A.Vogt, and S. Souramassing for technical support, B. Manil for his help at the beginning of the spectrometer construction, and the ASUR team from INSP. We thank L. Hudson, J. Gillaspy and T. Jach for helpful discussions.

References

Allison, S.K., 1932. The reflecting and resolving power of calcite for X-rays. Phys. Rev. 41, 1.

Allison, S.K., 1933. The natural widths of the K alpha X-ray doublet from 26FE to 47AG. Phys. Rev. 44, 63–72.

Allison, S.K., Williams, J.H., 1930. The resolving power of calcite for X-rays and the natural widths of the molybdenum Kα doublet. Phys. Rev. 35, 1476.

Amaro, P., 2011. Study of forbidden transitions in atomic systems (Ph.D. thesis). Universidade Nova de Lisboa.

Amaro, P., Schlesser, S., Guerra, M., Le Bigot, E.-O., Isac, J.-M., Travers, P., Santos, J.-P., Szabo, C.I., Gumberidze, A., Indelicato, P., 2012. Absolute measurement of the relativistic magnetic dipole transition energy in heliumlike argon. Phys. Rev. Lett. 109, 043005.

Anagnostopoulos, D.F., Biri, S., Boisbourdain, V., Demeter, M., Borchert, G., Egger, J., Fuhrmann, H., Gotta, D., Gruber, A., Hennebach, M., Indelicato, P., Liu, Y.W., Nelms, N., Simons, L.M., 2003a. Highly charged ions in exotic atoms research at PSI. Nucl. Instrum. Methods Phys. Res. B 205, 9–14.

Anagnostopoulos, D.F., Gotta, D., Indelicato, P., Simons, L.M., 2003b. Low-energy X-ray standards from hydrogenlike pionic atoms. Phys. Rev. Lett. 91, 240801.

Anagnostopoulos, D.F., Biri, S., Gotta, D., Gruber, A., Indelicato, P., Leoni, B., Fuhrmann, H., Simons, L.M., Stingelin, L., Wasser, A., Zmeskal, J., 2005. On the characterisation of a Bragg spectrometer with X-rays from an ECR source. Nuc. Instrum. Methods Phys. Res. A 545, 217.

Andreas, B., Azuma, Y., Bartl, G., Becker, P., Bettin, H., Borys, M., Busch, I., Gray, M., Fuchs, P., Fujii, K., Fujimoto, H., Kessler, E., Krumrey, M., Kuetgens, U., Kuramoto, N., Mana, G., Manson, P., Massa, E., Mizushima, S., Nicolaus, A., Picard, A., Pramann, A., Rienitz, O., Schiel, D., Valkiers, S., Waseda, A., 2011. Determination of the avogadro constant by counting the atoms in a ^{28}Si crystal. Phys. Rev. Lett. 106, 030801.

Antognini, A., Nez, F., Schuhmann, K., Amaro, F.D., Biraben, F., Cardoso, J.M.R., Covita, D.S., Dax, A., Dhawan, S., Diepold, M., Fernandes, L.M.P., Giesen, A., Gouvea, A.L., Graf, T., Hänsch, T.W., Indelicato, P., Julien, L., Kao, C.-Y., Knowles, P., Kottmann, F., Le Bigot, E.-O., Liu, Y.-W., Lopes, J.A.M., Ludhova, L., Monteiro, C.M.B., Mulhauser, F., Nebel, T., Rabinowitz, P., dos Santos, J.M.F., Schaller, L.A., Schwob, C., Taqqu, D., Veloso, J.F.C.A., Vogelsang, J., Pohl, R., 2013. Proton structure from the measurement of 2S–2P transition frequencies of muonic hydrogen. Science 339, 417–420.

Armstrong, B.H., 1967. Spectrum line profiles: the voigt function. J. Quant. Spectrosc. Radiat. Transf. 7, 61–88.

Artemyev, A.N., Shabaev, V.M., Yerokhin, V.A., Plunien, G., Soff, G., 2005. QED calculation of the $n=1$ and $n=2$ energy levels in He-like ions. Phys. Rev. A 71, 062104–062126.

Bearden, J.A., 1931a. Absolute wave-lengths of the copper and chromium K-series. Phys. Rev. 37, 1210.

Bearden, J.A., 1931b. The grating constant of calcite crystals. Phys. Rev. 38, 2089.

Bearden, J.A., 1932. Status of X-ray wavelengths in minutes of the new haven meeting, June 23–25, 1932. Phys. Rev. 41, 399.

Bearden, J.A., Thomsen, J.S., 1971. The double-crystal X-ray spectrometer: corrections, errors, and alignment procedure. J. Appl. Cryst. 4, 130.

Becker, P., Dorenwendt, K., Ebeling, G., Lauer, R., Lucas, W., Probst, R., Rademacher, H.-J., Reim, G., Seyfried, P., Siegert, H., 1981. Absolute measurement of the (220) lattice plane spacing in a silicon crystal. Phys. Rev. Lett. 46, 1540–1543.

Beyer, H.F., Deslattes, R.D., Folkmann, F., LaVilla, R.E., 1985. Determination of the 1s Lamb shift in one-electron argon recoil ions. J. Phys. B: At. Mol. Opt. Phys. 18, 207–215.

Beyer, H.F., Indelicato, P., Finlayson, K.D., Liesen, D., Deslattes, R.D., 1991. Measurement of the 1s Lamb-shift in hydrogen like nickel. Phys. Rev. A 43, 223–227.

Bieth, C., Bouly, J.L., Curdy, J.C., Kantas, S., Sortais, P., Sole, P., Vieux-Rochaz, J.L., 2000. Electron cyclotron resonance ion source for high currents of mono- and multicharged ion and general purpose unlimited lifetime application on implantation devices. Rev. Sci. Instrum. 71, 899–901.

Biri, S., Valek, A., Suta, T., Takacs, E., Szabo, C., Hudson, L.T., Radics, B., Imrek, J., Juhasz, B., Palinkas, J., 2004. Imaging of ECR plasma with a pinhole X-ray camera. Rev. Sci. Instrum. 75, 1420–1422.

Bonse, U., Hart, M., 1965. An X-ray interferometer. Appl. Phys. Lett. 6, 155.

Bragg, W.L., James, R.W., Bosanquet, C.H., 1921. XXIX. The intensity of reflexion of X-rays by rock-salt. Philos. Mag. Ser. 6 41, 309–337.

Brennan, S., Cowan, P.L., 1992. A suite of programs for calculating X-ray absorption, reflection, and diffraction performance for a variety of materials at arbitrary wavelength. Rev. Sci. Instrum. 63, 850–854.

Briand, J.P., Mossé, J.P., Indelicato, P., Chevallier, P., Girard-Vernhet, D., Chétioui, A., Ramos, M.T., Desclaux, J.P., 1983a. Spectroscopy of hydrogenlike and heliumlike argon. Phys. Rev. A 28, 1413–1417.

Briand, J.P., Tavernier, M., Indelicato, P., Marrus, R., Gould, H., 1983b. High precision spectroscopic studies of Lymanα lines of Hydrogenlike iron: a measurement of the 1s Lamb-shift. Phys. Rev. Lett. 50, 832.

Briand, J.P., Tavernier, M., Marrus, R., Desclaux, J.P., 1984. High-precision spectroscopic study of heliumlike iron. Phys. Rev. A 29, 3143.

Bruhns, H., Braun, J., Kubiček, K., Lopez-Urrutia, J.R.C., Ullrich, J., 2007. Testing QED screening and two-loop contributions with He-Like ions. Phys. Rev. Lett. 99, 113001–113004.

Campbell, J.L., Papp, T., 2001. Widths of the atomic K-N7 levels. At. Data Nucl. Data Tables 77, 1–56.

Chantler, C.T., 1995. Theoretical form factor, attenuation, and scattering tabulation for $Z=1$–92 from $E=1$–10 eV to $E=0.4$–1.0 MeV. J. Phys. Chem. Ref. Data 24, 71–643.

Chantler, C.T., 2000. Detailed tabulation of atomic form factors, photoelectric absorption and scattering cross section, and mass attenuation coefficients in the vicinity of absorption edges in the soft X-ray ($Z=30$–36, $Z=60$–89, $E=0.1$ keV–10 keV), addressing convergence issues of earlier work. J. Phys. Chem. Ref. Data 29, 597–1056.

Chantler, C.T., 2011. Detailed Tabulation of Atomic Form Factors, Photoelectric Absorption and Scattering Cross Section, and Mass Attenuation Coefficients for $Z=1$–92 from $E=1$–10 eV to $E=0.4$–1.0 meV.

Chantler, C.T., Kinnane, M.N., Gillaspy, J.D., Hudson, L.T., Payne, A.T., Smale, L.F., Henins, A., Pomeroy, J.M., Tan, J.N., Kimpton, J.A., Takacs, E., Makonyi, K., 2012. Testing three-body quantum electrodynamics with trapped Ti^{20+} ions: evidence for a z-dependent divergence between experiment and calculation. Phys. Rev. Lett. 109, 153001.

Chantler, C.T., Laming, J.M., Silver, J.D., Dietrich, D.D., Mokler, P.H., Finch, E.C., Rosner, S.D., 2009. Hydrogenic Lamb shift in Ge^{31+} and the fine-structure Lamb shift. Phys. Rev. A 80, 022508.

Chantler, C.T., Paterson, D., Hudson, L.T., Serpa, F.G., Gillaspy, J.D., Takacs, E., 2000. Absolute measurement of the resonance lines in heliumlike vanadium on an electron-beam ion trap. Phys. Rev. A 62, 042501-1–042501-13.

CODATA, 2011. Internationally recommended values of the fundamental physical constants 2010. ⟨http://physics.nist.gov/cuu/Constants/index.html⟩.

Compton, A.H., 1917. Reflection coefficient of a monochromatic X-rays from rock salt and calcite. In: Minutes of the Washington Meeting, vol. 10, p. 95.

Compton, A.H., 1931. A precision X-ray spectrometer and the wave length of Mo K alpha. Rev. Sci. Instrum. 2, 365–376.

Compton, A.H., Allison, S.K., 1935. X-rays in Theory and Experiment, 2nd ed. D. Van Nostrand Company, Inc., Toronto New York London.

Costa, A.M., Martins, M.C., Parente, F., Santos, J.P., Indelicato, P., 2001. Dirac–Fock transition energies and radiative and radiationless transition probabilities for Ar^{9+} to Ar^{16+} ion levels with K-shell holes. At. Data Nucl. Data Tables 79, 223–239.

Darwin, C.G., 1914a. LXXVIII. The theory of X-ray reflexion. Part II. Philos. Mag. Ser. 6 27, 675–690.

Darwin, C.G., 1914b. XXXIV. The theory of X-ray reflexion. Philos. Mag. Ser. 6 (27), 315–333.

Davis, B., Purks, H., 1927. Measurement of the Mo.K doublet distances by means of the double X-ray spectrometer. Proc. Natl. Acad. Sci. 13, 419–422.

Davis, B., Purks, H., 1928. Additional lines in the K series of molybdenum and the natural breadth of spectral lines. Proc. Natl. Acad. Sci. 14, 172.

Davis, B., Stempel, W.M., 1921. An experimental study of the reflection of X-rays from calcite. Phys. Rev. 17, 608.

Deslattes, R., Kessler , E., Indelicato, P., de Billy, L., Lindroth, E., Anton, J., 2003. X-ray transition energies: new approach to a comprehensive evaluation. Rev. Mod. Phys. 75, 35–99.

Deslattes, R.D., 1967. Two-crystal, vacuum monochromator. Rev. Sci. Instrum. 38, 616–620.

Deslattes, R.D., Beyer, H.F., Folkmann, F., 1984. Precision X-ray wavelength measurements in heliumlike argon recoil ions. J. Phys. B: At. Mol. Opt. Phys. 17, L689–L694.

Deslattes, R.D., Cowan, P.L., LaVilla, R.E., 1982. Multi-vacancy effects in argon K-spectra. In: AIP Conference Proceedings, no. 94, 100–104.

Deslattes, R.D., Henins, A., 1973. X-ray to visible wavelength ratios. Phys. Rev. Lett. 31, 972–975.

Deslattes, R.D., Kessler, E.G., Sauder, W.C., Henins, A., 1980. Remeasurement of g-ray reference lines. Ann. Phys. 129, 378–434.

Deslattes, R.D., Kessler Jr., E.G., Owens, S., Black, D., Henins, A., 1999. Just how perfect can a perfect crystal be?. J. Phys. D: Appl. Phys. 32, A3–A7.

Deslattes, R.D., LaVilla, R.E., Cowan, P.L., Henins, A., 1983. Threshold studies of a multivacancy process in the Kβ region of argon. Phys. Rev. A 27, 923–933.

Deutsch, M., Förster, E., Hölzer, G., Härtwig, J., Hämäläinen, K., Kao, C.-C., Huotari, S., Diamant, R., 2004. X-ray spectrometry of copper: new results on an old subject. J. Res. Natl. Inst. Stand. Technol. 109.

Deutsch, M., Gang, O., Hämäläinen, K., Kao, C.C., 1996. Onset and near threshold evolution of the Cu Kα X-ray satellites. Phys. Rev. Lett. 76, 2424.

Deutsch, M., Hölzer, G., Härtwig, J., Wolf, J., Fritsch, M., Förster, E., 1995. Kα and Kβ emission spectra of copper. Phys. Rev. A 51, 283–296.

Douysset, G., Khodja, H., Girard, A., Briand, J.P., 2000. Highly charged ion densities and ion confinement properties in an electron-cyclotron-resonance ion source. Phys. Rev. E 61, 3015–3022.

Ferroglio, L., Mana, G., Massa, E., 2008. Si lattice parameter measurement by centimeter X-ray interferometry. Opt. Express 16, 16877–16888.

Fujii, K., Waseda, A., Kuramoto, N., Mizushima, S., Becker, P., Bettin, H., Nicolaus, A., Kuetgens, U., Valkiers, S., Taylor, P., Paul, D.B., Mana, G., Massa, E., Matyi, R., Kessler Jr., E.G., Hanke, M., 2005. Present state of the Avogadro constant determination from silicon Crystals with natural isotopic compositions. IEEE Trans. Instrum. Measur. 54, 854–859.

Geller, R., 1996. In Electron Cyclotron Resonance Ion Sources and ECR Plasmas. Bristol, Institute of Physics.

Guerra, M., Amaro, P., Szabo, C.I., Gumberidze, A., Indelicato, P., Santos, J.P., 2013. Analysis of the charge state distribution in an ECRIS Ar plasma using high-resolution X-ray spectra. J. Phys. B: At. Mol. Opt. Phys. 46, 065701.

Gumberidze, A., Attia, D., Szabo, C.I., Indelicato, P., Vallette, A., Carmo, S., 2009. Trapping of highly charged ions with an electrostatic ion trap. J. Phys. Conf. Ser. 163, 012110.

Gumberidze, A., Trassinelli, M., Adrouche, N., Szabo, C.I., Indelicato, P., Haranger, F., Isac, J.-M., Lamour, E., Bigot, E.-O.L., Merot, J., Prigent, C., Rozet, J.-P., Vernhet, D., 2010. Electronic temperatures, densities, and plasma X-ray emission of a 14.5 GHz electron-cyclotron resonance ion source. Rev. Sci. Instrum. 81, 033303.

Hart, M., 1968. An Ångström ruler. J. Phys. D: Appl. Phys. 1, 1405.

Henke, B.L., Gullikson, E.M., Davis, J.C., 1993. X-Ray Interactions: Photoabsorption, Scattering, Transmission, and Reflection at $E=50$–$30{,}000$ eV, $Z=1$–92. At. Data Nucl. Data Tables 54, 181–342.

Hölzer, G., Förster, E., Klöpfel, D., Beiersdorfer, P., Brown, G.V., López-Urrutia, J.R.C., Widmann, K., 1998. Absolute wavelength measurement of the Lyman-α transitions of hydrogenic Mg^{11+}. Phys. Rev. A 57, 945.

Hudson, L., 2000. Private Communication.

Hölzer, G., Fritsch, M., Deutsch, M., Härtwig, J., Förster, E., 1997. Kα1,2 and Kβ1,3 X-ray emission lines of the 3d transition metals. Phys. Rev. A 56, 4554–4568.

Indelicato, P., 1983. Contribution à l'étude spectroscopique de transitions doublement excitées du fer heliumoïde. Thèse de troisième cycle Université Pierre et Marie Curie.

Indelicato, P., Boucard, S., Covita, D.S., Gotta, D., Gruber, A., Hirtl, A., Fuhrmann, H., Bigot, E.-O.L., Schlesser, S., Santos, J.M.F.D., Simons, L.M., Stingelin, L., Trassinelli, M., Veloso, J., Wasser, A., Zmeskal, J., 2007. Highly charged ion X-rays from electron-cyclotron resonance ion sources. Nucl. Instrum. Methods Phys. Res. A 580, 8–13.

Indelicato, P., Gorceix, O., Tavernier, M., Briand, J.P., Marrus, R., Prior, M., 1986a. Experimental and theoretical study of QED corrections in the ground state of heliumlike iron. Z. Phys. D 2, 149.

Indelicato, P., Le Bigot, E.-O., Trassinelli, M., Gotta, D., Hennebach, M., Nelms, N., David, C., Simons, L.M., 2006. Characterization of a charge-coupled device array for Bragg spectroscopy. Rev. Sci. Instrum. 77, 043107–043110.

Indelicato, P., Tavernier, M., Briand, J.P., Liesen, D., 1986b. Experimental study of relativistic correlations and QED effects in heliumlike krypton ions. Z. Phys. D 2, 249.

James, R.W., 1948. The Optical Principles of the Diffraction of X-rays of The crystalline state, vol. II. G. Bell and Sons, LTD, London.

Jian, H., Qingguo, Z., 2007. An exact calculation of the Voigt spectral line profile in spectroscopy. J. Opt. A: Pure Appl. Opt. 9, 565.

Kessler, E., J., Deslattes, R.D., Henins, A., 1979. Wavelength of the W Kα1 X-ray line. Phys. Rev. A 19, 215–218.

Kessler, E.G., Deslattes, R.D., Girard, D., Schwitz, W., Jacobs, L., Renner, O., 1982. Mid-to-high-Z precision X-ray measurements. Phys. Rev. A 26, 2696–2706.

Kessler, E.G., Henins, A., Deslattes, R.D., Nielsen, L., Arif, M., 1994. Precision comparison of the lattice parameters of silicon monocrystals. J. Res. Natl. Inst. Stand. Technol. 99, 1–18.

Kessler, E.G., Owens, S.M., Henins, A., Deslattes, R.D., 1999. Silicon lattice comparisons related to the Avogadro project: uniformity of new material and surface preparation effects. IEEE Trans. Instrum. Measur. 48, 221–224.

Kissel, L., 2000. Rtab: the Rayleigh scattering database. Radiat. Phys. Chem. 59, 185–200.

Kubiček, K., Braun, J., Bruhns, H., Lopez-Urrutia, J.R.C., Mokler, P.H., Ullrich, J., 2012. High-precision laser-assisted absolute determination of X-ray diffraction angles. Rev. Sci. Instrum. 83, 013102.

Le Bigot, E.O., Boucard, S., Covita, D.S., Gotta, D., Gruber, A., Hirtl, A., Fuhrmann, H., Indelicato, P., Santos, J.M.F.D., Schlesser, S., Simons, L.M., Stingelin, L., Trassinelli, M., Veloso, J.F.C.A., Wasser, A., Zmeskal, J., 2009. High-precision X-ray spectroscopy in few-electron ions. Phys. Scr. T134, 014015.

Lugovskaya, O.M., Stepanov, S.A., 1991. Calculation of the polarizabilities of crystals for diffraction of X-ray on the continuous spectrum at wavelengths of 0.1–10 AA. Sov. Phys. Crystallogr. 36, 478–481.

Luther, G.G., Deslattes, R.D., Towler, W.R., 1984. Single axis photoelectronic autocollimator. Rev. Sci. Instrum. 55, 747–750.

Martins, M.C., Costa, A.M., Santos, J.P., Indelicato, P., Parente, F., 2001. Interpretation of X-ray spectra emitted by Ar ions in an electron cyclotron resonance ion source. J. Phys. B 34, 533–543.

Martins, M.C., Marques, J.P., Costa, A.M., Santos, J.P., Parente, F., Schlesser, S., Le Bigot, E.-O., Indelicato, P., 2009. Production and decay of sulfur excited species in an electron-cyclotron-resonance ion-source plasma. Phys. Rev. A 80, 032501.

Massa, E., Mana, G., Ferroglio, L., Kessler, E.G., Schiel, D., Zakel, S., 2011. The lattice parameter of the 28 Si spheres in the determination of the Avogadro constant. Metrologia 48, S44.

Massa, E., Mana, G., Kuetgens, U., 2009a. Comparison of the INRIM and PTB lattice-spacing standards. Metrologia 46, 249.

Massa, E., Mana, G., Kuetgens, U., Ferroglio, L., 2009b. Measurement of the lattice parameter of a silicon crystal. New J. Phys. 11, 053013.

McSkimin, H.J., 1953. Measurement of elastic constants at low temperatures by means of ultrasonic waves-data for silicon and germanium single crystals, and for fused Silica. J. Appl. Phys. 24, 988–997.

Mohr, P.J., Taylor, B.N., Newell, D.B., 2008. CODATA recommended values of the fundamental physical constants: 2006. Rev. Mod. Phys. 80, 633.

Mooney, T., Lindroth, E., Indelicato, P., Kessler, E., Deslattes, R.D., 1992. Precision measurements of K and L transitions in xenon: experiment and theory for the K, L and M levels. Phys. Rev. A 45, 1531–1543.

Mäckel, V., Klawitter, R., Brenner, G., Crespo López-Urrutia, J.R., Ullrich, J., 2011. Laser spectroscopy on forbidden transitions in trapped highly charged Ar^{13+} ions. Phys. Rev. Lett. 107, 143002.

Nye, J.F., 1957. Physical Properties of Crystals. Oxford University Press, Oxford, England

Okada, Y., Tokumaru, Y., 1984. Precise determination of lattice parameter and thermal expansion coefficient of silicon between 300 and 1500 K. J. Appl. Phys. 56, 314–320.

Paros, J.M., Weisbord, L., 1965. Flexure hinges. Mach. Des. 37, 151.

Pohl, R., Antognini, A., Nez, F., Amaro, F.D., Biraben, F., Cardoso, J.M.R., Covita, D.S., Dax, A., Dhawan, S., Fernandes, L.M.P., Giesen, A., Graf, T., Hänsch, T.W., Indelicato, P., Julien, L., Kao, C.-Y., Knowles, P., Bigot, E.-O.L., Liu, Y.-W., Lopes, J.A.M., Ludhova, L., Monteiro, C.M.B., Mulhauser, F., Nebel, T., Rabinowitz, P., dos Santos, J.M.F., Schaller, L.A., Schuhmann, K., Schwob, C., Taqqu, D., Veloso, J.F.C. A., Kottmann, F., 2010. The size of the proton. Nature 466, 213–216.

Press, W.H., Flannery, B.P., Teukolsky, S.A., Vetterling, W.T., 1986. Numerical Recipes. Cambridge University Press, Cambridge

Prins, J.A., 1930. Die Reflexion von Röntgenstrahlen an absorbierenden idealen Kristallen. Z. Phys. 63, 477–493.

Sanchez del Rio, M., Dejus, R.J., 2004a. Status of XOP: an X-ray optics software toolkit. In: SPIE, vol. 5536, pp. 171–174.

Sanchez del Rio, M., Dejus, R.J., 2004b. XOP 2.1—A new version of the X-ray optics software toolkit. In: AIP Conference Proceedings, vol. 705, pp. 784–787.

Sanchez del Rio, M., Dejus, J., 1998. Xop: Recent developments. In: SPIE proceedings, p. 3448.

Santos, J.P., Costa, A.M., Marques, J.P., Martins, M.C., Indelicato, P., Parente, F., 2010. X-ray spectroscopy analysis of electron cyclotron-resonance ion source plasmas. Phys. Rev. A 82, 962516.

Santos, J.P., Martins, M.C., Costa, A.M., Indelicato, P., Parente, F., 2008. X-ray spectra emitted by Cl14+ ions in ECRIS plasmas. Vacuum 82, 1522–1524.

Santos, J.P., Martins, M.C., Costa, A.M., Marques, J.P., Indelicato, P., Parente, F., 2011. Production and decay of chlorine ion excited species in an electron cyclotron resonance ion source plasma. Phys. Scr. 2011, 014005.

Schwarzschild, M.M., 1928. Theory of the double X-ray spectrometer. Phys. Rev. 32, 162.

Schweppe, J., Deslattes, R.D., Mooney, T., Powell, C.J., 1994. Accurate measurement of Mg and Al Ka1,2 X-ray energy profiles. J. Electron Spectrosc. Relat. Phenom. 67, 463.

Schödel, R., Bönsch, G., 2001. Recent development in traceable dimensional measurements. In: Decker, J.E., Brown, N. (Eds.), Proceedings of SPIE, vol. 4401, pp. 54–62.

Soria Orts, R., Crespo, J.R., L.-U., Bruhns, H., González Martínez, A.J., Harman, Z., Jentschura, U.D., Keitel, C.H., Lapierre, A., Tawara, H., Tupitsyn, I.I., Ullrich, J., Volotka, A.V., 2007. Zeeman splitting and g factor of the $1s^22s^22p\ ^2P_{3/2}$ and $^2P_{1/2}$ levels in Ar^{13+}. Phys. Rev. A 76, 052501.

Stepanov, S., X0h on the web, ⟨http://sergey.gmca.aps.anl.gov/x0h.html⟩, 2013.

Szabo, C.I., Amaro, P., Guerra, M., Schlesser, S., Gumberidze, A., Santos, J.P., Indelicato, P., 2013. Reference free, high-precision measurements of transition energies in few electron argon ions. In: CAARI. AIP Conference Proceedings, Fort Worth, Texas, vol. 1525, pp. 68–72.

Szabo, C.I., Indelicato, P., LeBigot, E.-O., Vallette, A., Amaro, P., Guerra, M., Gumberidze, A., 2012. Progress on precision measurements of inner shell transitions in highly charged ions at an ECR ion source. In: The 17th International Conference On Atomic Processes in Plasmas (ICAPIP), Belfast, vol. 1438. American Institute of Physics, pp. 236–239.

Tavernier, M., Briand, J.P., Indelicato, P., Liesen, D., Richard, P., 1985. Measurement of the 1s Lamb shift of Hydrogenlike Krypton. J. Phys. B: At. Mol. Opt. Phys. 18, L327.

Trassinelli, M., Boucard, S., Covita, D.S., Gotta, D., Hirtl, A., Indelicato, P., Bigot, O.L., Santos, J.M.F.D., Simons, L.M., Stingelin, L., Veloso, J.F.C.A., Wasser, A., Zmeskal, J., 2007. He-like argon, chlorine and sulfur spectra measurement from an electron cyclotron resonance ion trap. J. Phys. Conf. Ser. 58, 129.

Waasmaier, D., Kirfel, A., 1995. New analytical scattering-factor functions for free atoms and ions. Acta Crystallogr. Sec. A 51, 416–431.

Wagner, E., Kulenkampff, H., 1922. Die Intensität der Reflexion von Röntgenstrahlen verschiedener Wellenlänge an Kalkspat und Steinsalz. Ann. Phys. 373, 369–413.

Williams, J.H., 1932. A correction to wave-length measurements with the double-crystal spectrometer. Phys. Rev. 40, 636.

Williams, J.H., Allison, S.K., 1929. Design of a double X-ray spectrometer. J. Opt. Soc. Am. 18, 473–478.

Zachariasen, W.H., 1967. Theory of X-ray Diffraction in Crystals. Dover Publications, New York